Results in Engineering 31 (2026) 111580

Contents lists available at ScienceDirect

Results in Engineering

journal homepage: www.sciencedirect.com/journal/results-in-engineering

Research paper

Structural safety assessment of a piston-type wavemaker under varying frequency and stroke conditions

Semin Kaya [a,*], Ahmet Kuscuoglu [a], Gulenay Alevay Kilic [b]

[a] Department of Mechanical Engineering, Engineering Faculty, Balikesir University, Balikesir, 10145, Turkiye
[b] Department of Electrical and Energy, Yalova University, Yalova, 77200, Turkiye

ARTICLE INFO

Keywords:
Piston-type wavemaker
Finite element analysis
Von Mises stress
Modal analysis
Structural integrity

ABSTRACT

The structural behaviour of piston-type wave generators under repeated hydrodynamic and inertial loads is a critical design parameter for the safe and long-term operation of laboratory-scale wave flumes. This study develops a finite element-based structural design and safety assessment methodology for laboratory-scale piston-type wavemakers, validated through multi-step numerical analysis and FPGA-controlled experimental motion confirmation. The methodology is demonstrated on a piston-type wave generator fabricated from S235JR structural steel for a 23 m × 1 m × 1 m wave flume, operating at 1.00 Hz with a maximum stroke of ±400 mm for a target wave range of H = 0.02–0.10 m and T = 0.8–2.5 s. Structural integrity was assessed via static, modal, and time-dependent analyses in ANSYS 2024 R1, with a parametric study spanning three frequencies and eight stroke conditions. In the static analysis, the design safety factor was 5.02 and stress levels remained below the infinite-life fatigue limit. Modal analysis yielded a first natural frequency 51 times the operating frequency, confirming the absence of resonance risk. Transient analysis showed that inertial effects increased the maximum von Mises stress by 45.4% to 68.1 MPa, with FS = 3.45. Across the full parametric envelope, the safety factor ranged from 2.90 to 5.02, satisfying the minimum design requirement in all cases. Results were verified through a three-tier framework comprising analytical benchmarking against classical plate theory, numerical self-consistency via mesh independence analysis, and operational confirmation of motion fidelity through FPGA-based position control experiments.

1. Introduction

In coastal and marine engineering, an understanding of wave mechanics is vital for the design of structures and the modelling of coastal processes. In this context, the literature contains a wide range of studies on physical wave generation, numerical modelling techniques, extreme wave conditions and wave-structure interactions. The simulation of marine conditions in a laboratory environment depends on the correct design of test tanks and wave generators (wavemakers). Beneduce has highlighted the importance of these facilities in marine engineering by examining the fundamental characteristics and historical development of test tanks [1]. In studies on various wave-generating mechanisms, Krvavica et al. proposed a new analytical equation for flap-type wave generators, which also includes wave-breaking limits [2]. In addition to piston and flap-type systems, various designs have also been developed for more complex waveforms. For example, Muarif et al. have investigated the mathematical modelling of snake-type wave generators to produce multi-directional waves [3]. Similarly, Gyongy et al. investigated the wave-generation capabilities of three-dimensional tanks by validating a hydrodynamic model for a curved, multi-pedal wave tank [4]. Lowell et al., who are working on plunger-type wave generators, analysed the sensitivity of parameters such as the wedge angle and water flow to wave generation [5]. Schmidt and Hedzielski, on the other hand, have discussed the kinematic properties of this mechanism by presenting displacement graphs of plunger movements with variable width [6].

In addition to traditional methods, a new generation of wave generators is also being designed, particularly for tsunami research. Beringer et al. have introduced a new wave generator system that operates using a bottom-tilting mechanism to simulate tsunami waves [7]. In another study, Hiraishi developed a hybrid system combining a piston, a current generator and a drop tank to simulate tsunamis and storm surges in shallow waters [8]. The precise generation of the desired waveform in wave channels and the suppression of reflections require advanced control strategies. Li has presented a theoretical framework

* Corresponding author.
E-mail address: skaya@balikesir.edu.tr (S. Kaya).

https://doi.org/10.1016/j.rineng.2026.111580
Received 17 May 2026; Received in revised form 4 June 2026; Accepted 14 June 2026
Available online 15 June 2026

for the control of wave-generating servo mechanisms and the generation of irregular wave trains [9]. Nouioui and Doğan, compared numerical and physical models by using the 'random phase method' to generate irregular waves suitable for the target JONSWAP spectrum using a piston-type wave generator [10]. The destructive effects of tsunamis are frequently studied through the lens of solitary wave mechanics. Krautwald et al. have generated real tsunami records (such as the 2004 Indian Ocean tsunami) in large-scale wave channels using piston-type wave generators, in the form of a combination of solitons [11]. Song et al. have numerically modelled the propagation characteristics of solitary waves in a stepped channel and their generation by piston motion using OpenFOAM [12].

In terms of structure-wave interactions, Lin et al. investigated the interaction between semi-submerged structures and solitary waves using the SPH method and analysed the wave loads [13]. In their doctoral thesis, Wang and Chan experimentally investigated the run-up heights of long waves and solitary waves and examined the effect of coated and uncoated surfaces [14]. Hess et al., on the other hand, experimentally measured the forces exerted by solitary impulse waves overtopping dams on vertical structures [15].

Statistical analysis of extreme events also plays an important role in wave mechanics. Canard et al. have proposed a new procedure for monitoring extreme wave statistics in experimental and numerical wave tanks [16]. In this context, Orszaghova et al. demonstrated that, in the case of focused wave groups climbing and breaching, the use of second-order wave generation signals rather than first-order ones reduces errors [17]. From a physical perspective, there are also theoretical discussions regarding non-linear dynamics, such as the formation of 'rogue' (giant) waves in deep water and modulation instability [18].

Renewable energy and offshore structures are among the main areas of application for wave research. Song et al. investigated modifications to tension-leg platforms (TLPs) and their behaviour under wave loads [19]. Yu et al. conducted an experimental study into the effects of sloshing on the behaviour of underwater soft-yoke mooring systems [20].

In the context of wave energy converters (WECs), Ahmed et al. analysed the performance of Oscillating Water Column (OWC) devices using computational fluid dynamics (ANSYS-CFD) [21]. Similarly, Gayathri et al. validated three-dimensional (3D) CFD models to investigate the effects of power transmission damping in OWC devices [22]. Thai Le and Truong, meanwhile, modelled the effect of wind-generated waves in open wave channel systems using ANSYS Fluent [23]. With regard to impact loads on coastal structures, Xu et al. experimentally investigated the wave impact forces (slamming) acting on the superstructures of coastal bridges using a piston-type wave generator [24]. In studies on coastal processes and sediment transport, Divinsky et al. investigated the effect of wave spectrum shape on the resuspension of bottom sediments [25]. Yan et al. experimentally analysed shoreline current profiles and their instabilities on gently sloping beaches [26]. Marin Diaz et al. investigated the role of eelgrass in sediment transport and resuspension [27].

The cost and scale effects of physical experiments have led researchers to develop Numerical Wave Tanks (NWT). Zhang et al. discussed the importance of numerical models (such as FLUENT) that incorporate viscous effects for investigating wave-structure interaction in permeable reef environments, as well as the classification of different numerical methods (FDM, FEM, BEM, FVM) [28]. In studies incorporating viscous effects, Singh and Roy simulated fully non-linear viscous wave generation by modelling the motion of piston and flap-type wave generators [29]. Similarly, Duan et al. created a numerical wave tank using STAR-CCM+ software by modelling piston and flap-type motions [30].

For larger-scale and three-dimensional simulations, Jia et al. integrated an L-type (bipartite) wave-generator configuration into a numerical model to simulate oblique and multidirectional waves [31]. Jung et al. ensured mass conservation in long-term simulations by developing a numerical wave tank based on shallow water equations, utilising a high-order WENO scheme and equipped with a piston-type wave generator [32]. Cho et al. numerically investigated the wave generation characteristics of bottom-tilting wave generators using the RANS-based Flow model and validated these results with laboratory data [33].

As an alternative approach, particle-based methods are also employed. Lee et al. have utilised SPH (Smoothed Particle Hydrodynamics) methods—a mesh-free technique—to model breaking waves and 'run-up' events in coastal regions. Jung et al. used the SPH method to simulate the propagation of linear water waves using a flap-type wave generator [34]. In studies on shallow water and Boussinesq models, Orszaghova et al. (2012) developed a hybrid model that uses Boussinesq equations for unbroken waves and non-linear shallow water equations for breaking waves [35]. Dong et al., on the other hand, conducted a comparative study on the generation and propagation of non-linear waves (solitary and cnoidal) in shallow water, evaluating the performance of the Green-Naghdi equations [36].

Despite the extensive literature on wave generation mechanisms and hydrodynamic performance, the structural integrity of wavemaker systems has received comparatively little attention. Existing studies predominantly focus on hydrodynamic efficiency, control strategies, and wave fidelity, whilst the mechanical design, stress distribution, and dynamic safety of the load-bearing structure under cyclic operational loading remain largely unaddressed. To the authors' knowledge, no previous study has presented a systematic FEM-based multi-step structural assessment encompassing static, modal, and transient analyses, combined with a quantitatively defined parametric operational safety envelope for a piston-type wavemaker. Furthermore, open hardware designs supported by structural safety data are scarce, limiting reproducibility and accessibility for research laboratories with constrained resources. The present study addresses these gaps directly.

The primary objective of this study is to develop and experimentally confirm a finite element-based structural design and safety assessment methodology for laboratory-scale piston-type wavemakers. The methodology is demonstrated on a piston-type wave generator fabricated from S235JR structural steel for a 23 m × 1 m × 1 m wave flume, through static, modal, and time-dependent FEM analyses verified by a three-tier framework comprising analytical benchmarking, mesh independence, and FPGA-controlled experimental motion validation. The specific contributions are: (i) a multi-step FEM structural assessment framework applied to a piston-type wavemaker, not previously reported in the open literature; (ii) a parametric operational safety envelope across 24 conditions (three frequencies × eight stroke levels); (iii) an EN 1993-1-9 FAT 71 fatigue assessment for the welded connections under cyclic loading; and (iv) an open hardware architecture with full structural safety documentation to support laboratory accessibility and reproducibility.

2. Material and method

2.1. Wave channel and design requirements

The piston-type wave generator was designed for a laboratory-scale wave flume located in the Hydraulics Laboratory of the Faculty of Engineering at Balıkesir University. The experimental setup shown in Fig. 1 is 23 m long, 1 m wide and has a maximum water depth of 1 m. The target operating range has been set as $H = 0.02$–0.10 m wave height and $T = 0.8$–2.5 s wave period [38]. The piston-type kinematic system was preferred because it offers higher volumetric displacement efficiency compared to a flap-type system in shallow and medium-depth waters, and because it eliminates bending moments concentrated in the hinge region, thereby ensuring a more homogeneous load distribution.

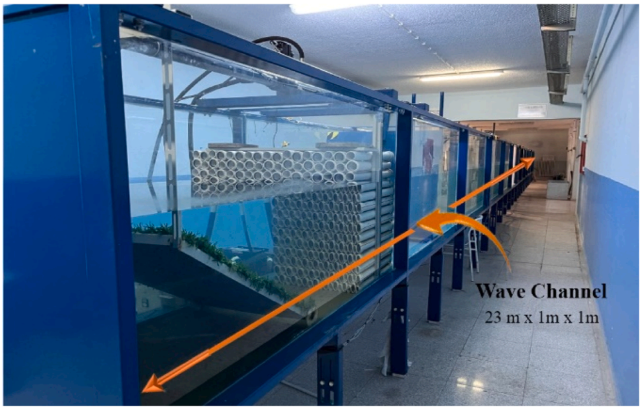

Fig. 1. Wave channel.

2.2. Mechanical design

The wave generator consists of three main subsystems: a rigid support frame, a linear guide mechanism and a piston plate. Fig. 2 shows the (a) schematic and (b) three-dimensional (3D) model of the designed system. The support frame is bolted to the wave channel structure and transmits all inertial and hydrodynamic loads to the foundation. The linear guide mechanism restricts the piston plate to translational motion only, thereby preventing rotational and lateral deflections during operation. The piston plate fully covers the 1 m × 1 m cross-section of the channel.

The piston movement in the system is sinusoidal in nature, and the repetitive movement frequency has been set at 1.00 Hz, considering the targeted wave period range and the dynamic stability of the mechanical system. The maximum stroke value is designed to be ±400 mm; this capacity ensures that the targeted wave height range is achieved at a water depth of 1 m, whilst allowing the hydrodynamic forces generated during piston movement to remain within controllable limits. All main structural components are manufactured from S235JR structural steel. This material was selected due to its weldability, predictable elastic behaviour under repeated loading, and ease of machining under workshop conditions.

2.3. Manufacturing and assembly

The selection of materials for structural systems is evaluated in terms of mechanical strength, workability and weld quality. It is known that fusion welding methods can lead to problems such as porosity and hot cracks [38]; therefore, S235JR steel was selected due to its reliable weldability under workshop conditions. Structural components were subjected to cutting, welding and CNC machining processes under workshop conditions in accordance with the tolerances specified in the design drawings. Upon completion of manufacture, all steel surfaces were cleaned of oil and oxide layers and subsequently coated with a corrosion-resistant paint suitable for use in a continuously high-humidity environment. As shown in Fig. 3, the system has been mounted at one end of a wave channel measuring 23 m × 1 m × 1 m; during the installation process, particular attention was paid to the parallelism of the piston plate with the channel walls and the vertical alignment of the guide columns. Alignment accuracy was verified by manual stroke tests prior to hydraulic connection; the fully assembled system is shown in Fig. 3(b).

2.4. Control architecture

The piston position is controlled via a double-acting hydraulic servo cylinder (total stroke 0–700 mm, operating range 300–700 mm)

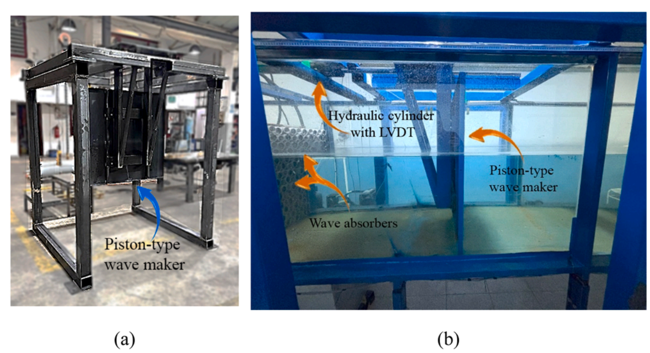

Fig. 3. Piston-type wave generator (a) production stage (b) side view of assembled state.

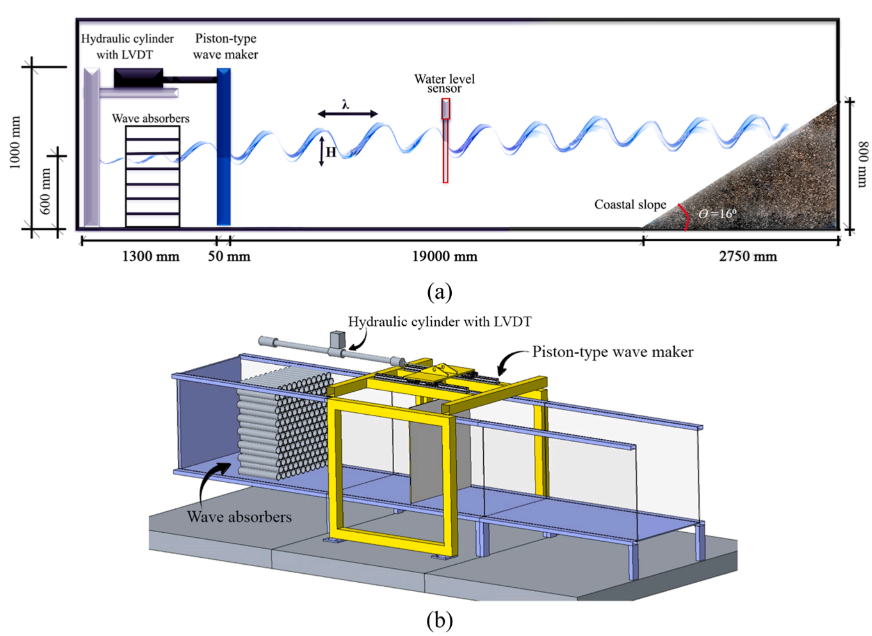

Fig. 2. Piston-type wave generator: (a) schematic diagram; (a) schematic (b) 3D representation.

equipped with a proportional valve and a linear position sensor. The control loop shown in Fig. 4 is implemented in LabVIEW software running on an FPGA-based real-time controller and provides cycle times in the order of microseconds. Wave generation commands are transmitted as sinusoidal position reference signals defined by amplitude, frequency and offset parameters, and are tracked via closed-loop position feedback [39].

2.5. Finite element analysis

The structural behavior of the piston-type wave generator was evaluated using static, modal and time-dependent analyses within the ANSYS 2024 R1 APDL environment. The finite element model consists of the piston plate, guide columns and upper support plate, whilst secondary connection details were neglected. The inertial loads generated during piston movement were converted into static equivalent body forces via the virtual work expression according to d'Alembert's principle. This approach provides a conservative upper limit that represents the structural effects of dynamic motion on the safe side and is widely used during the design phase. The global equilibrium equation obtained by applying the virtual work principle is expressed as follows [40]:

$$[K]\{u\} = \{F\} \tag{1}$$

Here, [K] is the global stiffness matrix, and {u} is the node degrees of freedom vector. The load vector {F} consists of three components. A gravitational acceleration of 9806.6 mm.s^{-2} has been applied to the entire structure as a body force. On the wet surface of the piston plate, a depth-dependent linear pressure distribution, as required by hydrostatic equilibrium, has been defined as a normal load in accordance with Pascal's law:

$$p(z) = \rho g\ (h - z) \tag{2}$$

the static equivalent body acceleration corresponding to the peak acceleration produced by a 1.00 Hz sinusoidal motion with an amplitude of 400 mm = 15.791 mm·s^{-2}. All loads were applied as nodal equivalent forces consistent with the element formulation. The hydrostatic pressure was defined as p(z) = ρgz, where ρ = 1000 kg·m^{-3} and z is the depth below the free surface, applied as a spatially varying normal surface load on the wetted face of the piston plate. A zero-displacement boundary condition has been defined at the upper connection points. The von Mises yield criterion, based on the Huber-von Mises-Hencky distortion energy theory, has been used in the assessment of structural damage. Compared to the maximum shear stress criterion, this criterion more accurately reflects the behaviour of ductile metallic materials under multi-axial stress conditions and is accepted as the standard design reference for welded steel structures. Mesh independence was verified via the peak von Mises stress prior to reporting the results. The von Mises yield criterion was adopted as the basis for the assessment of structural damage:

$$\sigma_{VM} = \sqrt{(\sigma_2^1 - \sigma_1\sigma_2 + \sigma_2^2)} \tag{3}$$

The resonance behaviour of the system has been investigated within the framework of conservative free vibration, assuming the structure to be linearly elastic and undamped. Under these assumptions, the equation of motion becomes homogeneous and reduces to the following eigenvalue problem:

$$\left([K] - \omega^2[M]\right)\{\varphi\} = \{0\} \tag{4}$$

Here, [M] is the mass matrix, ω is the natural angular frequency, and {φ} is the mode shape vector. To prevent resonance under repetitive piston loading, the natural frequencies must be sufficiently separated from the operating excitation frequency by a safety margin. To this end, the first six natural frequencies of the system were determined and compared with the 1.00 Hz operating frequency. For time-dependent analysis, the transient stress and strain behaviour arising during sinusoidal piston motion was investigated by solving the equation of motion derived from Newton's second law using the direct integration method [40]:

$$[M]\{\ddot{u}\} + [C]\{\dot{u}\} + [K]\{u\} = \{F(t)\} \tag{5}$$

Here, [C] is the damping matrix and {F(t)} is the time-dependent load vector. A sinusoidal displacement input with an amplitude of 200 mm was applied to the actuator connection point for a duration of 2 s; the contribution of the transient inertial effects arising during the piston's acceleration and deceleration phases to the structural response was tracked along the time axis.

2.5.1. FEM model composition

All structural components were discretised using three-dimensional solid elements assigned automatically by ANSYS Mechanical 2024 R1. Solid bodies with regular geometry were meshed with SOLID186 twenty-node quadratic hexahedral elements, whilst regions of complex geometry (guide column junctions, fillet transitions, and connection zones) were meshed with SOLID187 ten-node quadratic tetrahedral elements. No beam or shell elements were used; the full three-dimensional solid representation was retained throughout to capture stress gradients at connection details accurately. The global element size was set to 20 mm, with local refinement to 5 mm in the guide column-piston plate junction zones where stress concentrations are expected. All component interfaces were modelled using bonded contact pairs enforcing full displacement compatibility. The complete model composition is summarized in Table 1.

2.5.2. Mesh sensitivity analysis

The mesh structure used in the finite element model is shown in Fig. 5. Upon examining the enlarged views in Fig. 5, the guide columns with circular cross-sections have been modelled using an element

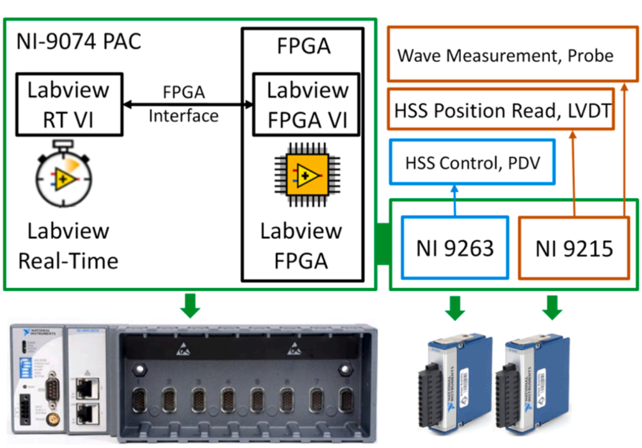

Fig. 4. Hydraulic system structure [39].

Table 1
The model composition.

Component	Element Type	Element Count	Average Element Size (mm)
Piston plate	SOLID186 (hexahedral)	~68,000	20
Guide columns	SOLID187 (tetrahedral)	~38,000	8–12
Support frame	SOLID186 (hexahedral)	~24,000	20
Connection/ junction zones	SOLID187 (tetrahedral)	~14,000	5
Total	SOLID186 + SOLID187	144,202	

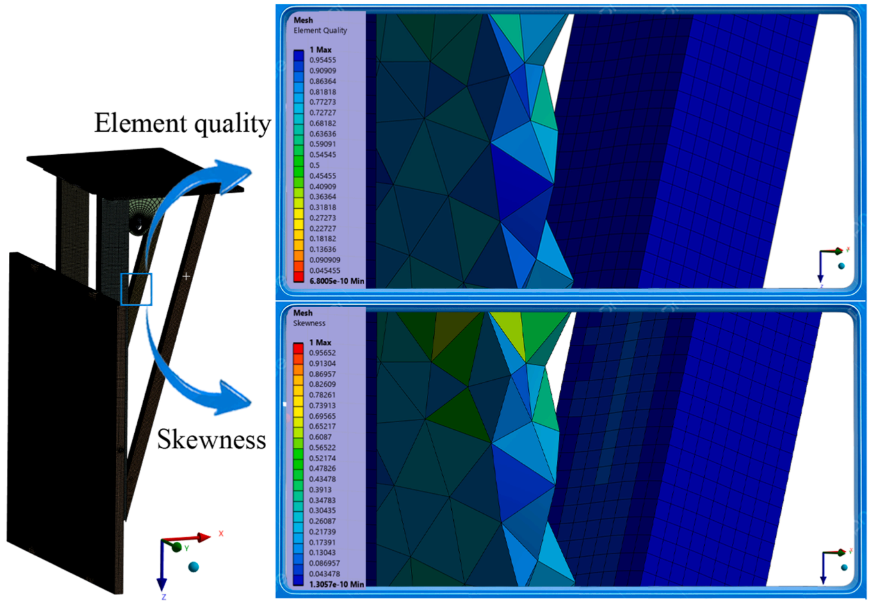

Fig. 5. Mesh quality assessment at the guide column–piston plate contact region: element quality and skewness.

arrangement configured to accurately represent the surrounding geometry, and that the contact surfaces between different structural components in the connection regions have been separated whilst maintaining mesh continuity. To assess the impact of the mesh structure created in the finite element model on solution reliability, element quality and skewness metrics were examined [41–43]. The mesh quality maps presented in Fig. 5 focus on the junction between the guide column and the piston plate, where geometric discontinuities and contact regions are concentrated. The element quality metric is defined between 0 and 1, with a value of 1 corresponding to perfect element geometry. It is observed that in the mesh structure used in the analysis, element quality largely ranges between 0.77 and 1.0. The skewness metric, on the other hand, indicates the degree of deviation from the ideal element geometry, where a value of 0 corresponds to perfect geometry and a value of 1 corresponds to completely distorted element geometry. It was determined that skewness values remained within the range of 0–0.43 across the majority of the mesh structure. The values observed in the triangular transition elements created as a necessity in the contact region remain within acceptable limits for ANSYS Mechanical and do not adversely affect solution stability. The combined evaluation of element quality and skewness values confirms that the generated mesh structure possesses sufficient geometric quality for structural analysis.

The mesh independence analysis presented in Fig. 6 demonstrates the effect of the number of elements on the maximum von Mises stress. It can be seen that when the number of elements is increased from approximately 30,000 to 75,000, the stress value rises rapidly from ~38.5 MPa to ~44 MPa. This behaviour indicates that stress concentrations in coarse mesh structures are underestimated due to insufficient resolution. At a mesh size of 144,202 elements, the stress value was obtained as 46.82 MPa; it was determined that increasing the number of elements to ~210,000 resulted in a change of only 0.7% in this value. This convergence behaviour demonstrates that the 144202-element mesh provides an optimal balance between computational efficiency and solution accuracy, and this mesh density was used in all subsequent analyses.

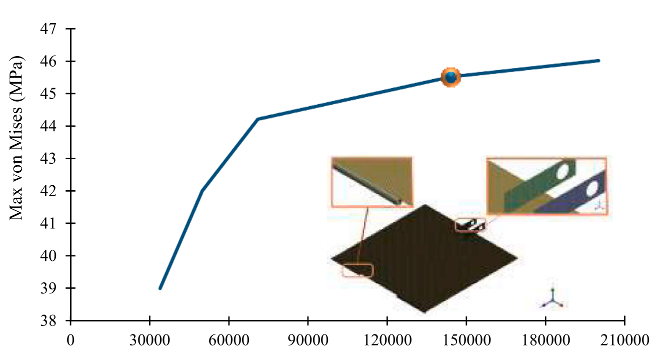

Fig. 6. Mesh sensitivity analyses.

2.6. Dimensionless structural performance parameters

To eliminate the dependence of structural analysis results on dimensional quantities, to evaluate the deviation from design criteria within a single framework, and to ensure comparability with different geometries or loading conditions, the key outputs obtained from static, modal and time-dependent analyses have been expressed in the form of dimensionless parameters. The five selected dimensionless parameters represent, respectively, dynamic stability, the amplification of inertial effects, geometric stiffness, material utilisation efficiency and structural safety margin, and together provide a comprehensive assessment of the system's structural performance.

2.6.1. Frequency ratio (r)

The frequency ratio is defined as the ratio of the nominal operating frequency (f_{op}) to the system's first natural frequency (f_{n1}):

$$r = f_{op} \Big/ f_{n1} \tag{6}$$

r, frequency ratio is the principal dimensionless parameter governing the dynamic amplification characteristics in forced vibration theory. In a viscously damped single-degree-of-freedom (SDOF) system, the dynamic amplification factor approaches extremely large values as the frequency ratio converges to unity ($0.8 \leq r \leq 1.2$), thereby leading to a critical resonance condition and a substantial risk of structural failure. From a structural safety perspective, it is therefore essential that the operating frequency remains sufficiently separated from this critical resonance region by an adequate safety margin. Under the condition of $r \ll 1$, the system response approaches quasi-static behavior, and inertial effects become negligible. For systems subjected to repetitive harmonic excitation, such as piston-type wave generators, maintaining the frequency ratio below 0.5 is generally recommended in order to account for potential variations in operating frequency and to ensure reliable dynamic performance under practical operating conditions [44].

2.6.2. Dynamic amplification factor (DAF)

The dynamic amplification factor is defined as the ratio of the maximum equivalent stress obtained from the time-dependent analysis to the maximum equivalent stress obtained from the static analysis:

$$DAF = \sigma_{transient} / \sigma_{static} \tag{7}$$

The *DAF* quantifies the amplifying effect of the inertial forces generated during the acceleration and deceleration phases of the piston on the static stress value. A value of $DAF = 1.0$ indicates that dynamic effects do not contribute further to the static state, whilst values of $DAF > 1.0$ indicate that time-dependent inertial effects increase the static stress. Although the recommended *DAF* range for impact and dynamic loading conditions in steel structures is specified as 1.2–2.0, it is known that this value varies depending on the type of loading and the structural configuration [45,46]. If only static analysis is deemed sufficient during the design phase and time-dependent effects are disregarded, this can lead to stress estimates that are significantly lower than the actual structural response. Therefore, *DAF* functions as a design verification parameter that quantitatively demonstrates the necessity of using both static and time-dependent analyses in the structural assessment of dynamic systems.

2.6.3. Stiffness ratio (SR)

The stiffness ratio is defined as the ratio of the maximum structural deformation to the characteristic height (L) of the piston plate

$$SR = \delta_{max} .L^{-1} \tag{8}$$

SR expresses the relative magnitude of structural displacement in relation to the geometric dimensions and indicates the extent to which the plate geometry is maintained under operating conditions. In piston-type wave generators, distortion of the plate geometry causes the generated wave profile to deviate from the reference sinusoidal form and leads to increased measurement errors in wave height. In laboratory systems requiring precise wave generation, the $SR \leq 1/1000$ stiffness criterion is accepted as the maximum deformation limit that will not compromise wave generation accuracy [10]. Meeting this criterion is of decisive importance, particularly in the generation of long-period waves, for maintaining phase consistency between the piston movement and the wave profile.

2.6.4. Stress ratio

The stress ratio is defined as the ratio of the maximum working stress to the material's yield strength and indicates how close structural members are to their elastic behaviour limits:

$$\sigma_{max} / \sigma_{yield} \tag{9}$$

The onset of yielding in structural members marks the threshold for irreversible plastic deformation and potential damage. Whilst EN 1993-1-1 requires that this ratio remain below 1.0 during the verification of the elastic limit state, it is recommended that this limit be set significantly lower in systems operating under repeated loading to ensure fatigue life [45]. The stress ratio also provides information on the material utilisation efficiency of the current design; low values indicate potential for weight optimisation in the design, whilst high values indicate a reduction in the safety margin.

2.6.5. Safety margin (SM)

The safety margin expresses, in dimensionless form, the extent to which the safety factor (FS) exceeds the design target, and is defined as follows [47]:

$$SM = (FS - 1).FS^{-1} \tag{10}$$

In this definition, a value of $SM = 0$ indicates that the structure is at the very limit of the minimum safety condition ($FS = 1$), whilst a value of $SM = 1$ corresponds to infinite safety capacity. Unlike the absolute value of the safety factor, the safety margin directly indicates the proportional magnitude of the unused structural capacity and allows for a normalised comparison with different safety factor targets. The minimum safety factor $FS \geq 2$, set as the design target, is equivalent to the limit $SM \geq 0.50$. *SM* values obtained above this limit demonstrate that the system maintains sufficient safety reserves under potential overload scenarios and long-term fatigue conditions.

2.7. Analytical verification of FEM results

To assess the reliability of the finite element model, the static structural results were independently verified against classical plate theory. The combined equivalent surface load was derived from the hydrostatic pressure distribution and the inertial body force corresponding to the applied acceleration of 15.791 $mm{\cdot}s^{-2}$, yielding a total equivalent uniform pressure of 0.00545 N/mm^2. The piston plate assembly, with plan dimensions of 1000 mm × 1000 mm, was idealized as a uniformly loaded square plate with all four edges clamped. Rather than using the nominal plate thickness alone, an equivalent bending stiffness thickness of 35 mm was adopted to represent the composite stiffness of the piston plate assembly, which derives its rigidity not only from the plate itself but also from the guide column connections, support frame continuity, and welded junction zones. This equivalent thickness is consistent with the effective stiffness implied by the FEM deformation field and reflects the contribution of the full structural assembly to out-of-plane resistance.

For a clamped square plate under uniform pressure, maximum deflection and maximum bending stress are given by classical thin-plate theory. The analytically computed maximum deflection of 0.796 mm is in reasonable agreement with the FEM result of 0.712 mm, providing qualitative support that the FEM loading and boundary conditions are physically consistent. Given the idealizations inherent in the plate analogy, this comparison serves as a qualitative lower-bound reference rather than a quantitative validation. The discrepancy is attributed to the simplifications inherent in the plate analogy: the analytical model treats the plate as uniformly supported on all four edges, whereas the FEM model captures the actual structural continuity through guide column connections, diagonal bracing, and contact interactions at the junction zones, all of which contribute additional stiffness not present in the idealised boundary conditions.

The analytically predicted maximum stress of 23.5 MPa is lower than the FEM peak value of 45.5 MPa. This difference is expected and physically consistent: classical plate theory yields the nominal bending stress in the plate field, while the FEM captures localised stress concentrations at the guide column–piston plate connections, where load transfer produces elevated stresses that plate theory cannot represent. The FEM peak stress therefore reflects the true structural demand at the critical connection zones, and the analytical result serves as a lower-bound reference for the distributed plate field. The level of agreement between the two methods confirms that the FEM model boundary conditions and loading definitions are physically consistent, and that the computed deformation field is within the range predicted by closed-form theory.

Experimental confirmation of the control system performance is provided in Fig. 7, which presents the reference and measured piston position signals recorded during operation at 1.00 Hz with a stroke amplitude of ±50 mm under FPGA-based real-time position control. As shown in Fig. 7(a), the measured displacement trace closely follows the sinusoidal reference signal throughout the recorded period, with no observable phase lag or amplitude attenuation. The visual agreement

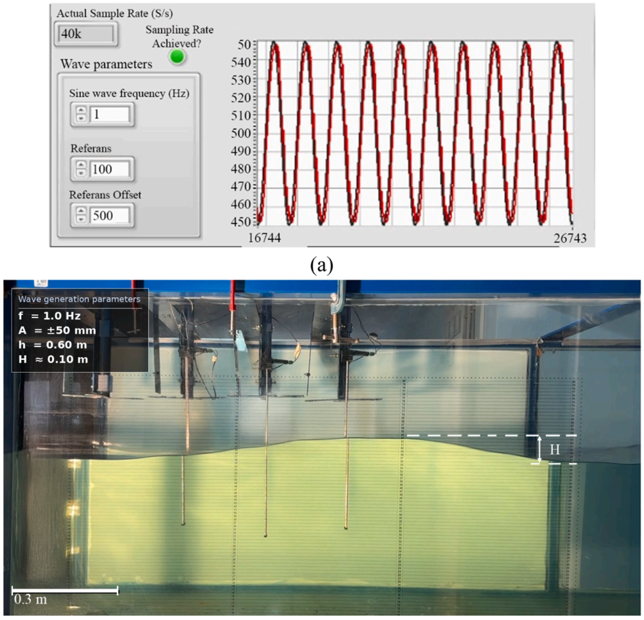

Fig. 7. Experimental piston-type wavemaker performance: (a) reference (black) and measured (red) piston position signals at 1.00 Hz, ±50 mm stroke amplitude under FPGA-based real-time control; (b) progressive wave generated in the flume under the same operating conditions [37,39].

between the two signals confirms that the hydraulic actuator faithfully tracks the prescribed motion profile under continuous cyclic loading. The physical realization of the designed wave generation is further evidenced in Fig. 7(b), which shows a well-formed progressive wave propagating along the flume under the same operating conditions. The wave crest is clearly distinguishable, and the free surface profile exhibits no irregular breaking or surface disturbance, confirming that the mechanical system operates with low vibration and stable dynamic behaviour. Taken together, the analytical verification of the FEM deformation field, the close correspondence between finite element and plate-theory predictions, and the experimental confirmation of position tracking accuracy establish a coherent three-tier verification framework for the structural and mechanical design presented in this study. It is noted that the experimental study confirms actuator position tracking and physical wave generation; direct measurement of structural stress or deformation under operating loads is acknowledged as a limitation and is identified as a priority for future work.

3. Results and discussion

3.1. Results of the static structural analysis

In the static structural analysis, the variable hydrostatic pressure loading conditions applied to the piston plate are shown in Fig. 8(a), and the pressure distribution is shown in Fig. 8(b). Upon examining the pressure distribution shown in Fig. 8(b), minimum values are reached in regions close to the free surface, whilst maximum values are reached as one approach the base. This distribution is fully consistent with Pascal's law, which predicts a linear increase in hydrostatic pressure with water depth. The maximum hydrostatic pressure value obtained on the wet surface of the piston plate as a result of the analysis is 0.0047 MPa; the fact that the pressure contours exhibit a uniform distribution with continuity along the surface confirms that the loading has been defined consistently on the model.

The colour scale illustrating the total deformation distributions shown in Figs. 9(a) and (b) indicates the magnitude of displacement occurring on the structural members. Examination of Fig. 8 reveals that the maximum displacement is concentrated in the middle-lower region of the piston plate. This region coincides with the area where the hydrostatic pressure load reaches its highest values, indicating that pressure-induced loads are directly reflected in the structural response. The maximum total deformation value obtained under static loading conditions is 0.78 mm; this value meets the L/1000 stiffness limit specified as the design criterion. In other words, the maximum displacement occurring in the system remains at a negligible level relative to the characteristic geometric dimensions, and no deformation occurs that would adversely affect wave generation sensitivity. The fact that deformation levels remain very low along the upper carrier plate and guide elements demonstrates that these regions exhibit high structural stiffness. The uniform and continuous distribution of deformation contours on the piston plate supports the conclusion that the loading and boundary conditions are defined consistently within the model.

When the von Mises stress distributions shown in Figs. 10(a) and (b) present the *xyz* axes from front and rear views—are evaluated together, it can be seen that the maximum equivalent stress is concentrated in the lower and central regions of the piston plate, in areas where hydrodynamic pressure loading and inertial effects caused by acceleration act

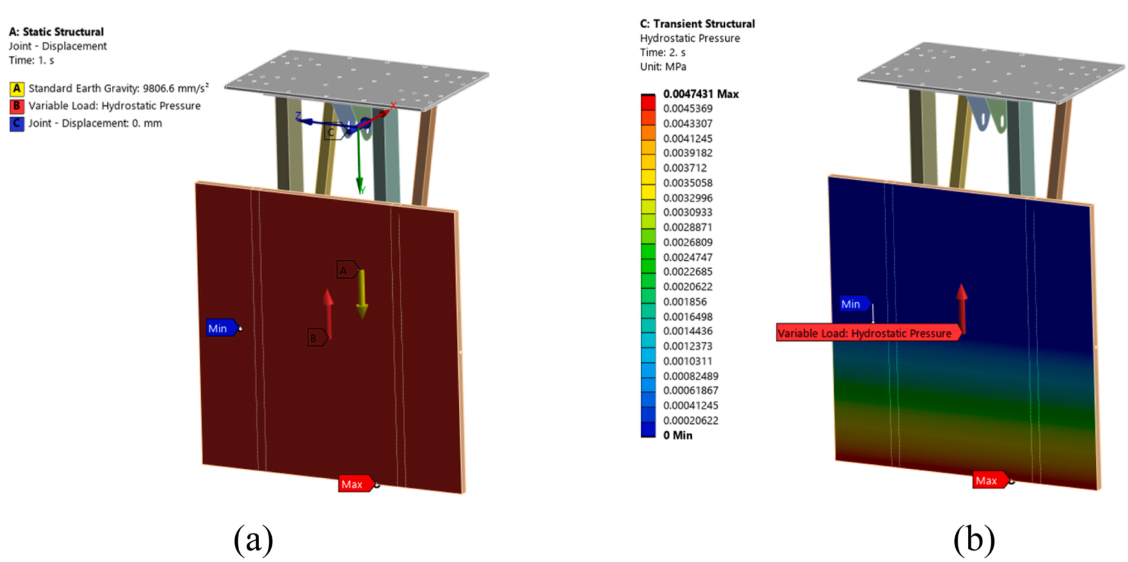

Fig. 8. Variable hydrostatic pressure applied to the piston plate (a); loading conditions; isometric view (b); pressure distribution.

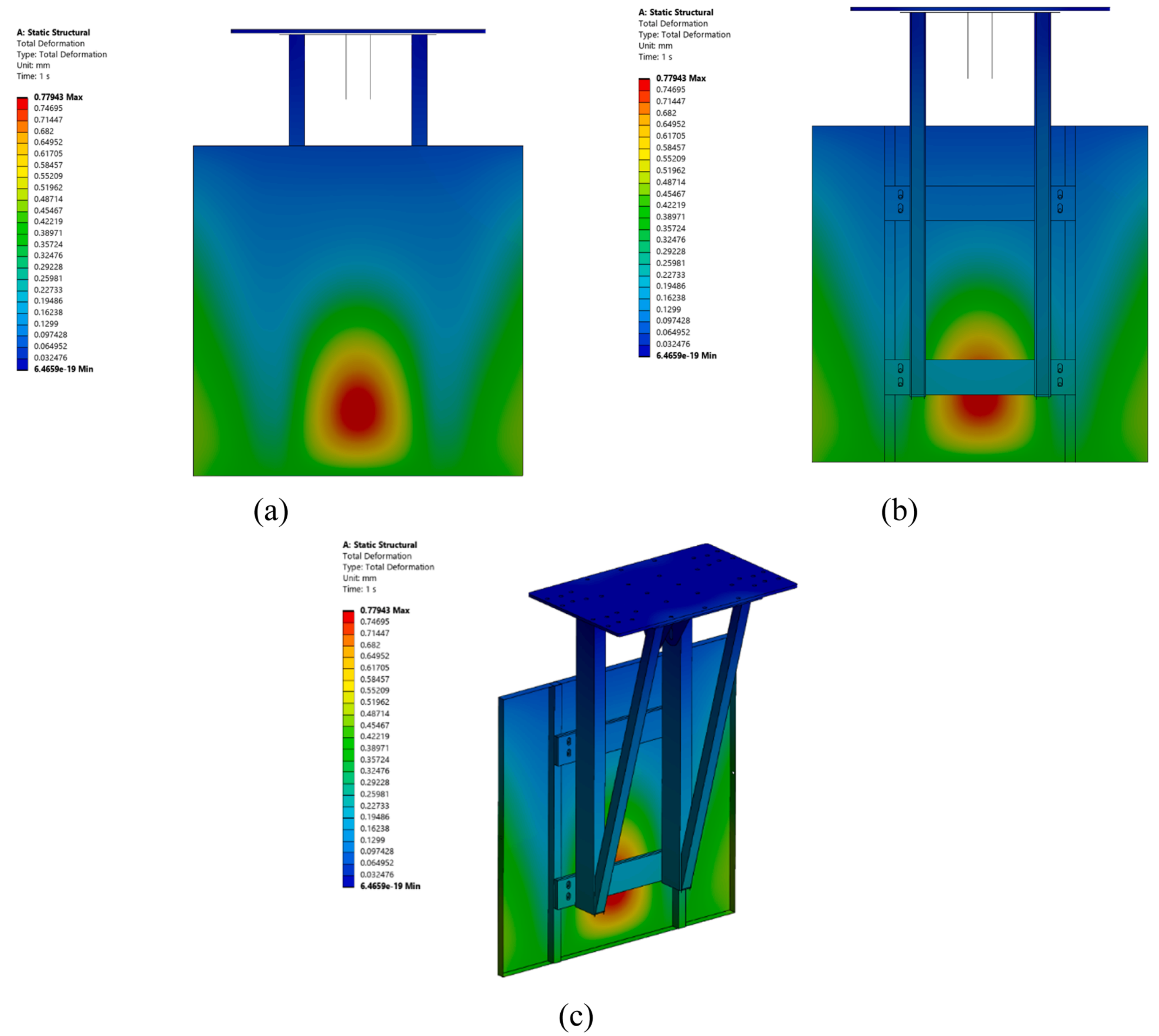

Fig. 9. Total deformation distributions (a) front view (b) back view.

together. The maximum von Mises stress obtained under static loading conditions is 46.82 MPa; this value corresponds to approximately one-fifth of the nominal yield strength (235 MPa) of S235JR structural steel. It is observed that the stress values measured at the marked nodal points are concentrated in the range of 18–20 MPa, indicating that the load transfer mechanism operates in a balanced manner throughout the structure. The relatively low stress levels along the guide elements and the upper support plate demonstrate that the loads generated during piston movement are distributed homogeneously within the structure. The fact that the stress contours exhibit a continuous distribution confirms that the connection and contact definitions have been consistently modeled in the analysis.

The maximum von Mises stress obtained, 46.82 MPa, is well below the nominal yield strength of S235JR steel, resulting in a design safety factor of $FS = 235/46.82 = 5.02$. This value is significantly higher than the minimum safety factor of 2 set as the design target, indicating that the system operates with a high safety margin under static loading conditions. A fatigue assessment was performed in accordance with EN 1993-1-9 using Detail Category FAT 71 [45], which corresponds to non-load-carrying fillet welds at the guide column–piston plate connections. The guide column profiles function as transverse attachments on the rear face of the piston plate, providing lateral and rotational restraint during sinusoidal piston motion; the cyclic loads are transmitted through the piston plate section itself rather than through these welds, confirming their classification as non-load-carrying fillet welds in accordance with EN 1993-1-9 [45]. A damage-tolerant assessment approach was adopted, consistent with the fail-safe character of the laboratory wavemaker structure, and a partial safety factor 1.00 was applied in accordance with EN 1993-1-9 [45].

The nominal stress range was taken as $\Delta\sigma = \sigma\_max - \sigma\_min$, where $\sigma\_min \approx 0$ under the one-directional piston loading cycle, yielding $\Delta\sigma$ equal to the peak von Mises stress in each case. Under nominal operating conditions (Case B4, ±200 mm stroke, 1.00 Hz), the stress range of 63.3 MPa remains below the FAT 71 reference fatigue strength of 71 MPa at 2×10^6 cycles, satisfying the infinite-life criterion. At the maximum design capacity (Case B8, ±400 mm), the stress range of 77.5 MPa marginally exceeds the FAT 71 threshold; however, as ±400 mm represents the upper design limit rather than a continuous operating condition, this

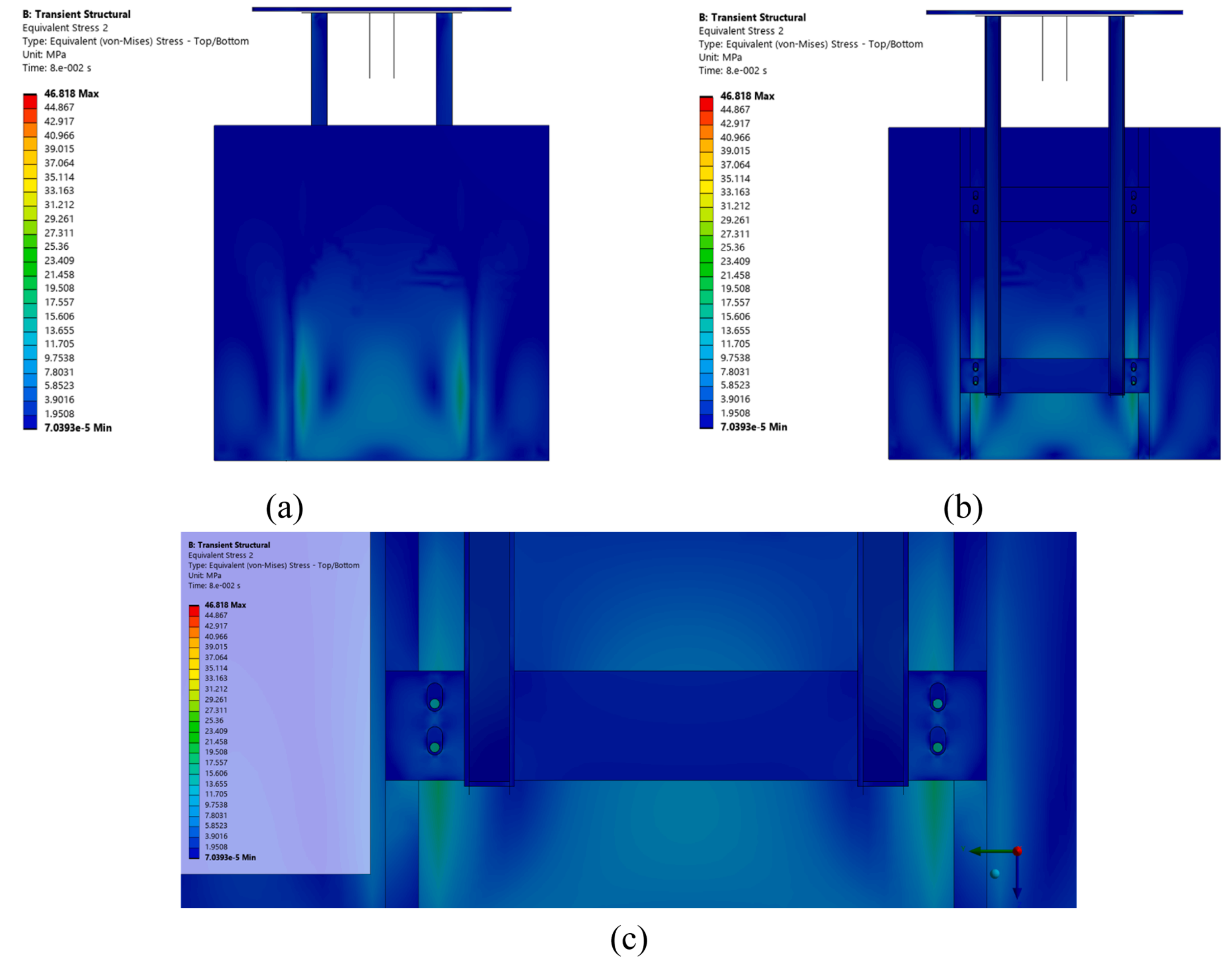

Fig. 10. Equivalent stress distributions (a) front view (b) back view (c) back close-up view.

exceedance does not govern the fatigue life under normal service. These results confirm that the structure operates within acceptable fatigue limits across the intended working envelope.

3.2. Modal analysis results

The results of the modal analysis, conducted to determine the system's natural frequencies and assess the risk of resonance under operating conditions, are presented in Fig. 11. The first natural frequency was determined to be 50.88 Hz, which corresponds to approximately 51 times the nominal operating frequency (1.00 Hz). Upon examining Fig. 11, it is observed that the natural frequencies exhibit a general increasing trend with mode order; however, this increase is not evenly distributed among the modes. The frequencies of the second and third modes are 56.95 Hz and 57.34 Hz, respectively, with a difference of only 0.39 Hz (0.7%). This closeness indicates that these two modes correspond to different vibration modes with similar structural stiffness-to-mass ratios. In the transition from the third to the fourth mode, however, the frequency rises from 57.34 Hz to 75.89 Hz, showing a distinct jump of 32.3%. This jump reflects a transition to a different vibration character where structural stiffness becomes dominant compared to the previous modes. From the fourth to the sixth mode, frequencies continue to increase by 14.8% and 10.0%, respectively; this indicates that the vibration character in the higher modes is becoming increasingly localized. The deformation normalized to the first mode is concentrated in the lower and lateral regions of the piston plate; the upper support plate and guide columns exhibit minimal deformation, demonstrating rigid-body behavior. The fact that all the first six modes are located at least 50 times farther from the 1.00 Hz operating frequency confirms that the system will not be exposed to any resonance risk under repetitive piston loading.

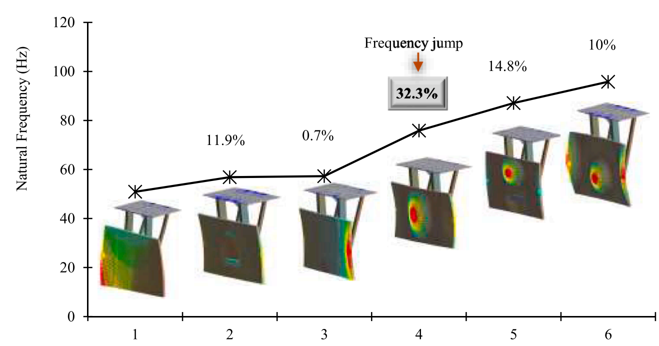

Fig. 11. Natural frequencies of the first six vibration modes of the piston-type wavemaker structure obtained from modal analysis.

An examination of the first six mode shapes presented in Fig. 12

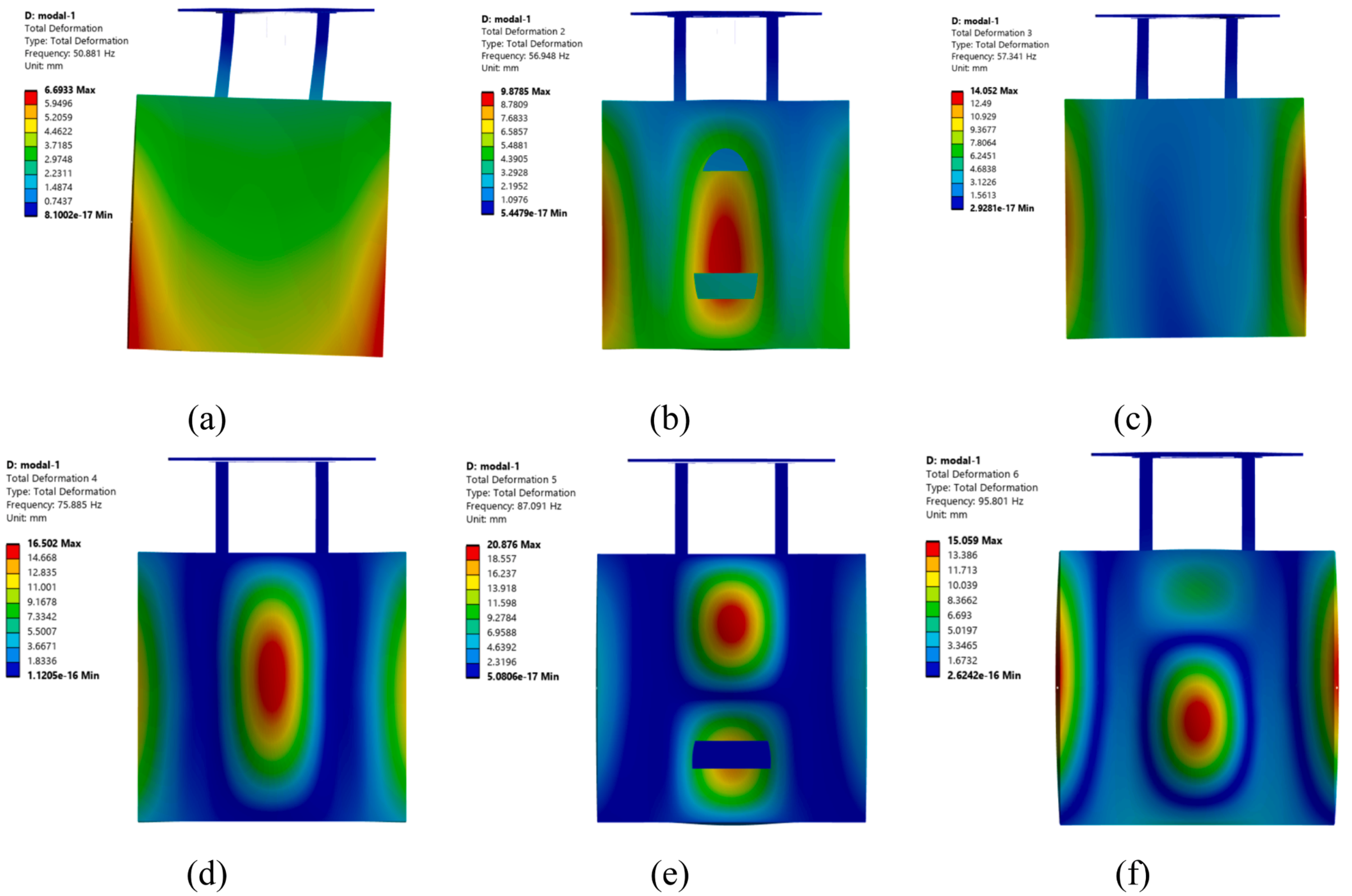

Fig. 12. First six mode shapes of the piston-type wavemaker structure: (a) Mode 1 – 50.88 Hz, (b) Mode 2 – 56.95 Hz, (c) Mode 3 – 57.34 Hz, (d) Mode 4 – 75.89 Hz, (e) Mode 5 – 87.09 Hz, (f) Mode 6 – 95.80 Hz.

reveals that each mode exhibits a distinct vibration characteristic. In the first mode (50.88 Hz), global translational behaviour concentrated at the lower corners of the piston plate is dominant; the upper support plate and guide columns exhibit minimal deformation consistent with the boundary conditions. In the second mode (56.95 Hz), an out-of-plane bending character with an oval lobe at the plate center is observed; this indicates a local vibration behavior with a higher energy content compared to the first mode. The third mode (57.34 Hz) reflects an antisymmetric bending character of the plate surface, and it is observed that the deformation distribution is divided into two regions with opposite phases relative to the plate axis. In the fourth mode (75.89 Hz), high-order bending behavior concentrated at the plate center becomes prominent; in the fifth mode (87.09 Hz), a more localized vibration character with horizontal bands is exhibited in the lower region of the plate. In the sixth mode (95.80 Hz), high-order local vibration behaviour with two distinct lobes becomes dominant, indicating that the vibration character in the higher modes is becoming increasingly localized. The fact that all modes are located far from the operating frequency (1.00 Hz) definitively confirms that the system will not be exposed to any resonance risk under repetitive piston loading.

3.3. Time-dependent analysis results

Upon examining the total deformation distributions presented in Fig. 13, the maximum displacement, at 200.8 mm, is concentrated in the lower-middle region of the piston plate. In the front view shown in Fig. 13(a), the deformation exhibits a symmetrical and continuous distribution across the piston plate surface, with the maximum value occurring in the lower region near the plate center. This situation is directly related to the dominant bending effect created by the hydrostatic pressure loading on the plate. In the rear view with the support frame shown in Fig. 13(b), it is observed that deformation levels remain quite low along the guide columns and the upper support plate, and that these regions exhibit high structural stiffness. The low deformation levels on the rear surface of the guide columns confirm that the piston movement is restricted to only the translational component and that the guide mechanism effectively prevents unwanted rotation and lateral deflections. Upon examining the detailed view of the lower region of the piston plate presented in Figs. 13(c) and (d), it is observed that the region of maximum deformation is concentrated in a central area near the lower edge of the plate. Gravitational acceleration of 9806.6 mm·s^{-2} was applied as a uniform body force to the entire assembly. The hydrostatic pressure was assigned as a spatially varying normal surface load on the wetted face of the piston plate, defined as $p(z) = \rho g z$, where $\rho = 1000$ kg·m^{-3}, g = 9806.6 mm·s^{-2}, and z is the depth below the free surface. The peak inertial body force corresponding to the maximum operating acceleration of 15,791 mm·s^{-2} was applied as a uniform body acceleration in the piston stroke direction. All loads were applied as nodal equivalent forces consistent with the element formulation. This region stands out as a critical area where both the hydrostatic pressure reaches its maximum value and inertia-induced loads most significantly affect the structural response. Due to the definition of a zero-displacement boundary condition at the upper connection points, the deformation exhibits a gradual increase profile from top to bottom; this is consistent with the system's global stiffness behaviour.

An examination of the time-dependent total deformation graph presented in Fig. 14 reveals that the system consistently and continuously tracks the sinusoidal displacement input. The deformation value exhibits a smooth increase from the initial position, reaching a peak value of 200.8 mm at approximately t = 2 s, and then decreases

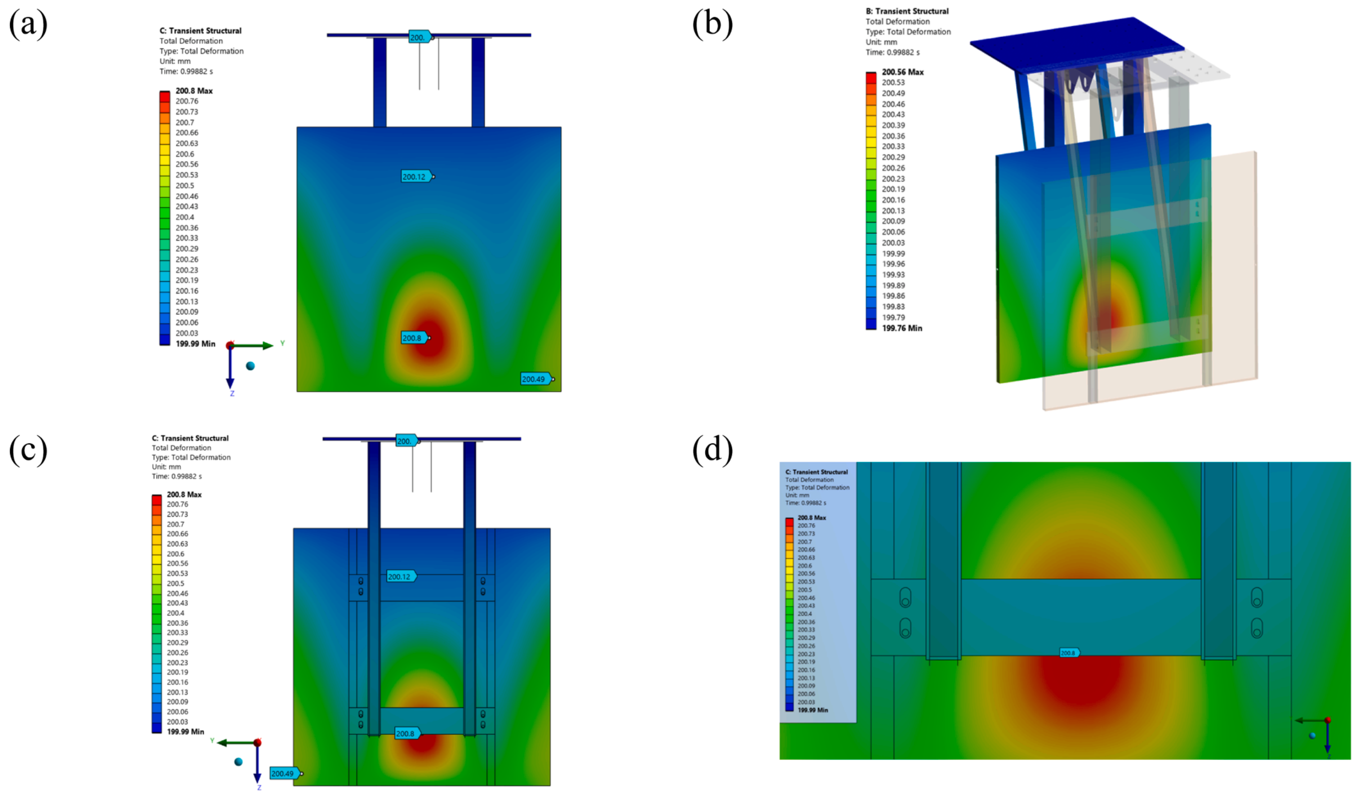

Fig. 13. Total deformation distribution under transient loading: (a) front view, (b) deformation displacement (c) back view with structural frame, (d) close-up of maximum deformation region on piston plate.

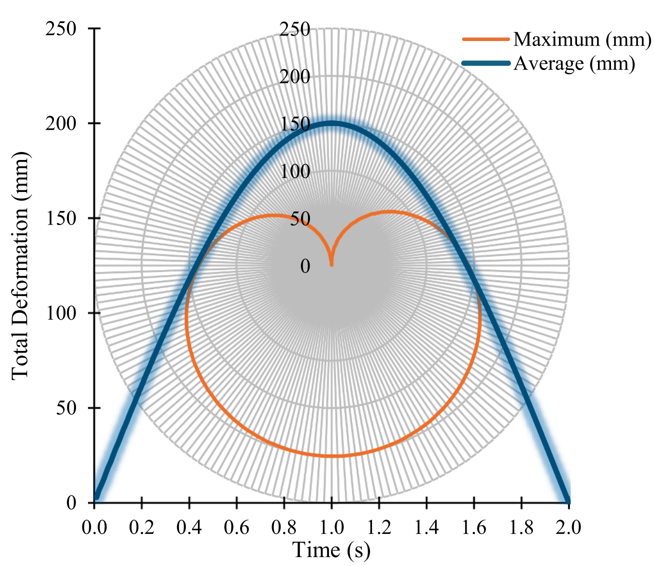

Fig. 14. Total deformation response over one complete piston cycle under sinusoidal displacement input.

symmetrically, returning to the initial position at the end of the cycle. This sinusoidal behavior confirms that the piston motion does not involve sudden changes in velocity or acceleration throughout the motion cycle and that the system's mechanical structure transmits the input signal in a predictable manner. The 0.4% deviation between the input amplitude of 200 mm and the maximum deformation of 200.8 mm indicates that the analysis model represents the displacement boundary condition with high accuracy. The fact that the deformation curve maintains its symmetric structure throughout the cycle and contains no instability or drift supports the stability of the numerical solution.

Upon examining the equivalent stress distributions presented in Fig. 15, it is observed that the maximum stress is concentrated in the upper connection regions of the guide columns. Under time-dependent loading conditions, the maximum equivalent stress is 68.1 MPa, representing a 45.4% increase compared to the static analysis result. This increase directly reflects the contribution of transient inertial effects arising during the piston's acceleration and deceleration phases to the structural response. In the front view presented in Fig. 15(a), stress concentration becomes evident in the lower regions of the piston plate, and areas where hydrostatic pressure and inertial effects act together emerge as critical regions. In the rear view with the support frame shown in Fig. 15(b), it is observed that the stress distribution along the guide columns exhibits a continuous and balanced character, while stress levels remain relatively low in the upper support plate regions. This indicates that the transient loads generated during piston movement are transferred to the superstructure in a balanced manner through the load-bearing elements. Upon examining the detailed view of the guide column connection regions presented in Fig. 15(c), it is observed that stress concentrations are particularly concentrated at the points where the columns meet the piston plate. These regions correspond to critical areas where load transfer is most intense at the moments when the piston changes direction and acceleration effects reach their maximum. However, the maximum stress value obtained corresponds to approximately one-third of the yield strength (235 MPa) of S235JR steel, and the design safety factor *FS* was calculated as 3.45. The fact that the stress contours exhibit a continuous distribution across all views confirms that the boundary conditions defined in the time-dependent analysis are consistently reflected in the solution.

The time-dependent von Mises stress plot shown in Fig. 16 illustrates the evolution of the instantaneous maximum and average stress values throughout the analysis period. During the initial transient phase of the analysis ($t < 0.15$ s), the maximum stress exhibits irregular oscillations

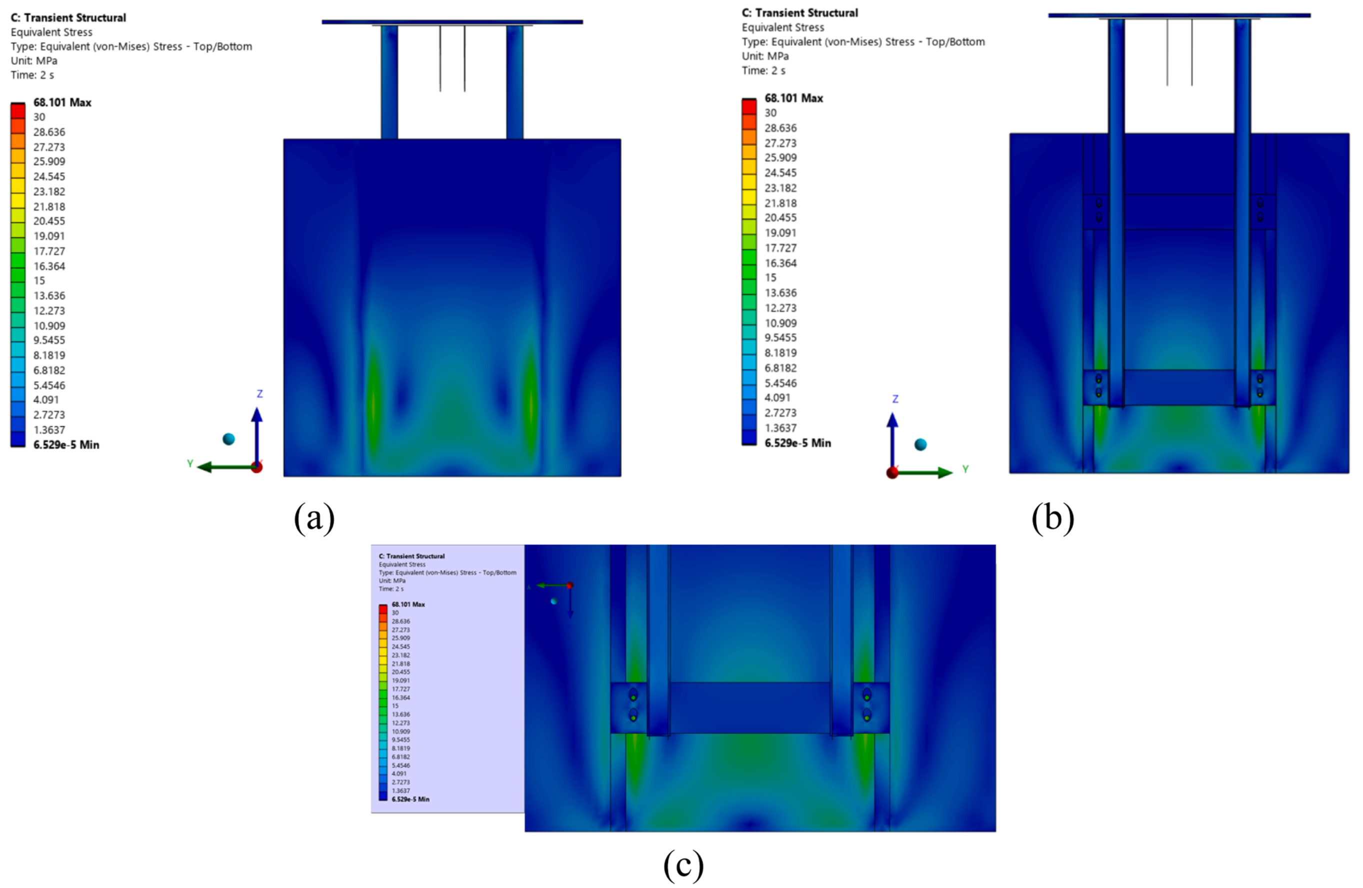

Fig. 15. Equivalent (von Mises) stress distribution under transient loading at t = 2 s (max. 68.1 MPa): (a) front view, (b) back view with structural frame, (c) close-up of stress concentration at guide column connections.

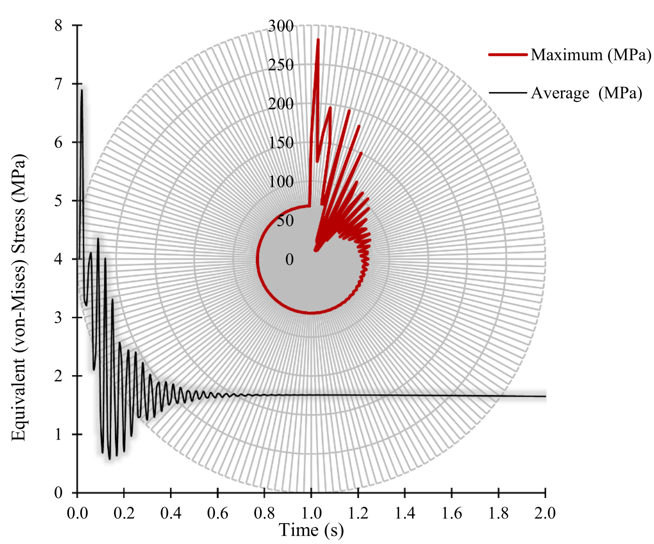

Fig. 16. Maximum and average equivalent (von Mises) stress time history during transient analysis.

in the range of 100–281.6 MPa. This behaviour is a result of the initial transient effect caused by the sudden application of sinusoidal motion from a zero-initial condition and does not represent actual steady-state operating conditions. Starting from t ≈ 0.3 s, the system stabilizes, and the maximum stress remains within the 63–80 MPa range. The steady-state maximum stress at t = 2 s is 68.1 MPa, and this value is the basis for the design safety factor calculation. The average stress curve ranges from 1.65 to 6.89 MPa throughout the analysis; this confirms that high stress values are concentrated in limited local regions of the structure, while the structure operates at low stress levels.

3.4. Dimensionless structural performance

To enable a comprehensive evaluation of the analysis results obtained within the scope of this study in terms of design criteria and to quantitatively demonstrate the relationships between different types of analysis, the key parameters derived from static, modal, and time-dependent analyses have been expressed in dimensionless form. The dimensionless parameters presented in Table 2 summarize the system's structural performance within a single framework; they also enable a comparative assessment of the design's distance from safety limits and its behavior under dynamic loading conditions.

The calculated frequency ratio, $r = 0.0197$, indicates that the nominal operating frequency corresponds to only 1.97% of the first natural frequency of the system. In forced vibration theory, the resonance region is commonly defined within the range of $0.8 \le r \le 1.2$, where the dynamic amplification factor reaches critical levels and may lead to severe

Table 2
Dimensionless structural performance parameters of the piston-type wavemaker.

Parameter	Symbol	Formula	Value
Frequency ratio	r	f_{op} / f_{n1}	0.0197
Dynamic amplification factor	DAF	$\sigma_{transient} / \sigma_{static}$	1.454
Stiffness ratio	SR	δ_{max} / L	7.8×10^{-4}
Stress ratio	—	$\sigma_{max} / \sigma_{yield}$	0.286
Safety margin	SM	$(FS - 1) / FS$	0.714

structural response amplification. The frequency ratio of the proposed system is located approximately 40 times below the lower bound of this critical resonance interval, clearly demonstrating that potential minor variations in the operating frequency are unlikely to adversely affect the structural response. This substantial separation from the resonance region confirms the dynamic stability and operational reliability of the designed system under practical service conditions.

The calculated dynamic amplification factor (*DAF*) of 1.454 indicates that time-dependent inertial effects increase the static stress response by approximately 45.4%. For steel structures subjected to dynamic loading conditions, the recommended *DAF* range is generally reported as 1.2–2.0 [47], and the obtained value remains well within these accepted engineering limits. This result confirms that the equivalent static loading approach provides a systematic degree of conservatism, while simultaneously demonstrating that transient dynamic effects produce a non-negligible increase in structural stresses that should be explicitly considered during the design assessment process. The findings therefore validate both the structural adequacy of the proposed system and the necessity of incorporating dynamic response analysis into the overall engineering evaluation.

SR, 7.8×10^{-4}, represents the ratio of the maximum deformation to the characteristic height of the piston plate. In laboratory systems requiring precise wave generation, the geometric stability of the piston plate is a parameter that directly affects wave profile accuracy, and the L/1000 limit is generally accepted as a stiffness criterion [10]. The *SR* value remains below this limit, indicating that the plate geometry will be maintained without distortion under operating conditions. The stress ratio of 0.286 indicates that the maximum operating stress reaches only 28.6% of the yield strength. According to EN 1993-1-1, the condition $\sigma_{Ed} / \sigma_{Rd} \leq 1.0$ must be satisfied in the elastic limit state verification; the obtained value remains well below this limit, confirming that the structural members operate within the elastic range [44]. The fact that the stress ratio remains at 0.286 also indicates significant potential for weight optimization within the current design geometry and serves as a reference point for future lightweighting efforts.

SM is 0.714, indicating that the system has 71.4% of its structural capacity unused. This value is significantly above the *SM*=0.50 limit required by the minimum *FS*=2 set as the design target, demonstrating that the system maintains an adequate safety margin under both nominal operating conditions and potential overload scenarios. A comprehensive evaluation of the five dimensionless parameters confirms that the designed piston-type wave generator meets all specified design criteria and demonstrates reliable structural performance for laboratory-scale coastal engineering applications.

3.5. Frequency-dependent structural response under parametric loading

To evaluate the sensitivity of the structural response to changes in operational frequency, a parametric study was performed across three excitation cases at 0.50, 1.00, and 1.50 Hz. For a sinusoidal piston motion with amplitude A and frequency f, peak acceleration scales, yielding inertial body loads of 1974, 7896, and 17,763 $mm \cdot s^{-2}$ for Cases A1, A2, and A3, respectively. These accelerations were applied as equivalent static body forces following the d'Alembert formulation, so that the structural demand from each frequency scenario could be isolated and compared directly. Total deformation and equivalent von Mises stress results for all three cases are summarised in Table 3. Total deformation increases monotonically with frequency. Maximum deformation rises from 0.763 mm at 0.50 Hz to 0.966 mm at 1.50 Hz, a 26.6% increase across the examined range. Average deformation values remain below 0.102 mm in all cases, confirming that elevated displacement is spatially confined to the lower central region of the piston plate where hydrostatic pressure is greatest. All three maximum deformation values remain below the 1.0 mm threshold corresponding to the L/1000 stiffness criterion for a 1 m plate height, indicating that geometric integrity of the piston plate is preserved throughout the full operational envelope.

Table 3
Total deformation and equivalent von Mises stress results for parametric frequency cases.

Case	Strok ($\pm$mm)	Acceleration ($mm.s^{-2}$)	Total deformation		
			Minimum (mm)	Maximum (mm)	Average (mm)
A1	200	1974	5.99E-17	0.76323	6.45E-02
A2	200	7896	7.56E-17	0.83915	7.79E-02
A3	200	17,765	1.71E-16	0.96567	0.10123
			Equivalent von Mises Stress		
Case		Acceleration ($mm.s^{-2}$)	Minimum (MPa)	Maximum (MPa)	Average (MPa)
A1	200	1974	3.95E-05	52.616	1.4508
A2	200	7896	2.37E-05	63.28	1.6894
A3	200	17,763	2.80E-05	81.049	2.1225

The minimum deformation values, on the order of 10^{-17} mm, are numerically bounded quantities associated with the fixed upper boundary nodes and carry no physical significance.

The equivalent von Mises stress follows the same frequency-dependent pattern. As shown in Fig. 17, maximum stress increases from 52.6 MPa at 0.50 Hz to 81.0 MPa at 1.50 Hz, a 54.0% rise over the same frequency range. The stress curve exhibits a noticeably steeper gradient at higher frequencies compared to the deformation curve, reflecting the quadratic dependence of inertial body force on frequency. Average stress values across the three cases remain between 1.45 and 2.12 MPa, confirming that elevated stresses are localised at the guide column connection zones rather than distributed uniformly across the structure. Even at the most demanding condition, the peak von Mises stress of 81.0 MPa does not exceed the yield strength of S235JR steel and remains within the infinite-fatigue-life regime widely adopted for welded structural steel.

The evolution of the safety factor with frequency is presented in Fig. 18. The factor of safety decreases from 4.47 at 0.50 Hz to 3.71 at 1.00 Hz and further to 2.90 at 1.50 Hz, tracing a consistent downward trend as inertial loading intensifies. All three values remain above the minimum design requirement of $FS \geq 2$, represented by the horizontal limit line in Fig. 18, confirming that the structure retains adequate safety reserves across the entire frequency range examined. The rate of decrease in safety factor accelerates with frequency, consistent with the quadratic growth of inertial body force, and indicates that frequencies substantially beyond 1.50 Hz would approach the design threshold more rapidly. The parametric results therefore define 1.50 Hz as a practical upper bound for structural safety under the current design configuration, while simultaneously demonstrating that the nominal operating frequency of 1.00 Hz provides a comfortable margin of $FS = 3.71$ above the minimum requirement.

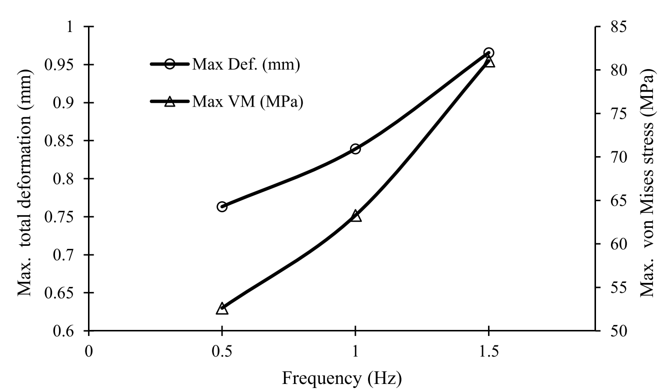

Fig. 17. Effect of operational frequency for cases.

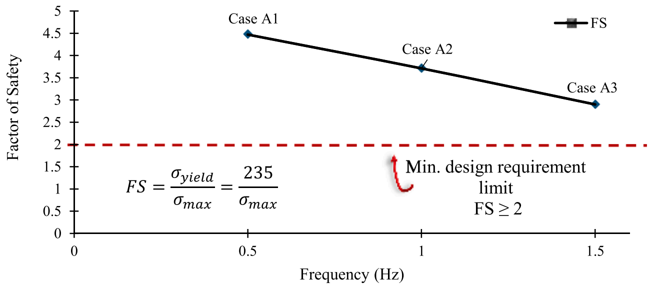

Fig. 18. Variation of factor of safety with operational frequency; horizontal line indicates the minimum design requirement $FS \geq 2$.

3.6. Structural response under varying stroke amplitude

To evaluate the effect of piston stroke amplitude on structural response at a fixed operating frequency of 1.00 Hz, eight cases were examined with stroke amplitudes ranging from ±50 mm to ±400 mm in 50 mm increments. Since the peak acceleration in sinusoidal piston motion scales linearly with amplitude, the static equivalent body forces between B1 and B7 vary in the range of 3948 mm·s^{-2} to 15,791 mm·s^{-2}. The results for total deformation and equivalent von Mises stress are presented in Table 4; when the variation of the structural response with stroke amplitude is examined, it is observed that the maximum total deformation increases regularly with stroke amplitude. The value of 0.763 mm in the B1 case rises to 0.940 mm in the B8 case; despite the stroke amplitude increasing fourfold, the increase in deformation remains at only 19.2%.

Fig. 19 shows that both curves exhibit a nearly perfectly linear increase along the stroke axis. The relatively flat course of the deformation curve indicates that the hydrostatic pressure loading remains the dominant component of the structural response in all cases, and that the inertia-induced loading makes only a limited contribution to this component. In all eight cases, the maximum deformation values remain below the L/1000 stiffness criterion limit applicable for a 1 m plate height. The equivalent von Mises stress exhibits a more pronounced increasing trend. The maximum stress increases from 52.6 MPa in Case B1 to 77.5 MPa in Case B8, and this 37.9% increase corresponds to approximately twice the increase in deformation. The fact that the average stress values remain below 2.1 MPa in all cases confirms that high-stress regions are limited to the guide column connection points and that the structure as a whole operates at low stress levels. The stress value of 77.5 MPa obtained at the design maximum stroke of ±400 mm approaches the upper threshold of the accepted fatigue limit for welded steel structures but does not exceed it.

Table 4
Total deformation and equivalent von Mises stress results for parametric stroke cases at 1.00 Hz.

Case	Strok (±mm)	Acceleration (mm.s^{-2})	Total deformation Minimum (mm)	Maximum (mm)	Average (mm)
B1	50	1974	5.22E-17	0.76323	6.45E-02
B2	100	3948	7.62E-17	0.78854	6.89E-02
B3	150	5922	1.26E-16	0.81384	7.34E-02
B4	200	7896	9.39E-17	0.83915	7.79E-02
B5	250	9870	5.24E-17	0.86446	8.24E-02
B6	300	11,844	1.18E-16	0.88977	8.69E-02
B7	350	13,817	9.70E-17	0.91507	9.15E-02
B8	400	15,791	9.19E-17	0.94038	9.64E-02
			Equivalent von Mises Stress		
Case	Strok (±mm)	Acceleration (mm.s^{-2})	Minimum (MPa)	Maximum (MPa)	Average (MPa)
B1	50	1974	3.95E-05	52.616	1.4508
B2	100	3948	2.81E-05	56.171	1.5285
B3	150	5922	1.88E-05	59.725	1.608
B4	200	7896	2.37E-05	63.28	1.6894
B5	250	9870	1.34E-05	66.835	1.7725
B6	300	11,844	1.00E-05	70.39	1.8572
B7	350	13,817	9.10E-06	73.943	1.9437
B8	400	15,791	1.43E-05	77.498	2.0321

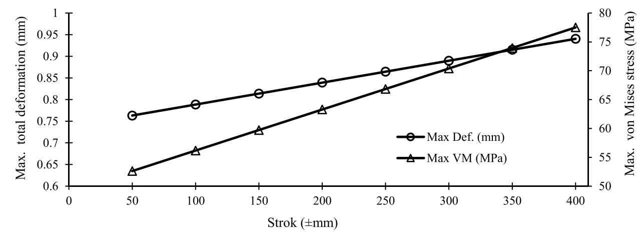

Fig. 19. Effect of piston stroke amplitude on maximum total deformation and maximum von Mises stress at 1.00 Hz.

The safety factor curve shown in Fig. 20 indicates that the *FS* value decreases steadily from 4.47 at B1 to 3.03 at B7 as the stroke amplitude increases. The monotonic decrease observed across the seven points exhibits a linear character and reflects the linear scaling of acceleration with amplitude. However, in all cases, the FS value remains well above the design target of $FS \geq 2$. Even at the design maximum stroke of ±400 mm, a safety margin of 1.5 times the minimum requirement is maintained with an *FS* value of 3.03. This result confirms that the system maintains sufficient structural safety margin even at full stroke capacity and that ±400 mm constitutes a safe operating limit under the current design configuration [48].

4. Conclusion

Laboratory-scale wave flumes form the fundamental experimental infrastructure for coastal and marine engineering research, and the mechanical reliability of wave generators determines both the accuracy of experimental results and the long-term operability of these systems. Although piston-type wave generators are widely preferred for shallow and medium-depth channels owing to their homogeneous load distribution and high volumetric efficiency, their structural behaviour under repeated hydrodynamic and inertial loading has not been systematically investigated. The present study addresses this gap by developing a finite element-based structural design and safety assessment methodology for laboratory-scale piston-type wavemakers, validated through multi-step numerical analysis and FPGA-controlled experimental motion confirmation. The methodology was demonstrated on a piston-type wave generator fabricated from S235JR structural steel for a 23 m × 1 m × 1 m wave flume, designed for a maximum stroke of ±400 mm at a nominal operating frequency of 1.00 Hz and a target wave range of H = 0.02–0.10 m and T = 0.8–2.5 s [39].

In the static structural analysis, the maximum von Mises stress under combined hydrostatic pressure and inertial loading was 46.82 MPa, corresponding to approximately one-fifth of the S235JR yield strength, with a design safety factor $FS = 5.02$. The maximum total deformation of

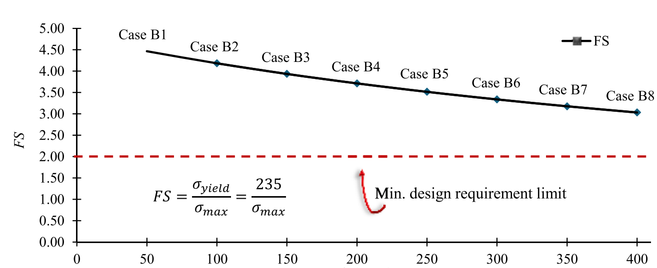

Fig. 20. Variation of factor of safety with piston stroke amplitude at 1.00 Hz; horizontal line indicates the minimum design requirement $FS \geq 2$.

0.78 mm remained below the L/1000 stiffness limit. A fatigue check performed in accordance with EN 1993-1-9 FAT 71 (non-load-carrying fillet weld) confirmed that the nominal operating stress range of 63.3 MPa at Case B4 (±200 mm stroke) falls below the reference fatigue strength of 71 MPa at 2×10^6 cycles, satisfying the infinite-life criterion across the intended working envelope.

Modal analysis yielded a first natural frequency of 50.88 Hz, 51 times higher than the operating frequency and corresponding to a frequency ratio r = 0.0197. All six modes examined maintain sufficient separation from the operating frequency, confirming that the structure is free from resonance risk under repetitive piston loading.

In the transient analysis, a 200 mm amplitude sinusoidal input produced a maximum displacement of 200.8 mm, deviating by only 0.4% from the prescribed signal. Transient inertial effects during the acceleration and deceleration phases raised the maximum von Mises stress to 68.1 MPa, corresponding to a *DAF* of 1.454, which falls within the 1.2–2.0 range accepted for steel structures, with $FS = 3.45$. Evaluation of the five dimensionless performance parameters ($r = 0.0197$, $DAF = 1.454$, $SR = 7.8 \times 10^{-4}$, stress ratio = 0.286, $SM = 0.714$) confirms that all design criteria are met with adequate safety margins.

In the frequency parametric study, operating frequencies of 0.5, 1.0, and 1.50 Hz were examined at a constant amplitude of ±200 mm. The maximum von Mises stress increased from 52.6 MPa to 81.0 MPa (54.0%) whilst the safety factor decreased from 4.47 to 2.90; the $FS \geq 2$ condition was satisfied in all cases. Given the quadratic scaling of acceleration with frequency, 1.50 Hz was identified as the practical upper operational limit for the present design. In the stroke parametric study, eight cases (B1–B8) were examined at 1.00 Hz with amplitudes from ±50 mm to ±400 mm in 50 mm increments. Maximum deformation increased linearly from 0.763 mm to 0.940 mm (23.2%) and maximum von Mises stress from 52.6 MPa to 77.5 MPa (47.3%), whilst the safety factor decreased monotonically from 4.47 to 3.03. A safety margin of 1.5 times the minimum requirement was maintained at the design maximum stroke of ±400 mm. Across both parametric studies, frequency variation produced a more severe effect on structural demand than stroke variation.

FEM results were assessed against classical plate theory as a qualitative lower-bound reference. The analytical deformation is in reasonable agreement with the FEM prediction; the residual difference reflects the additional stiffness contributions of the guide columns and support frame that the plate analogy cannot capture. Experimental studies conducted under FPGA-based real-time position control showed no phase lag or amplitude deviation between the reference and measured piston position signals, and physical wave generation was visually confirmed. The three-tier verification framework, comprising analytical benchmarking against plate theory, numerical self-consistency through mesh independence analysis, and operational confirmation of motion fidelity, supports the structural and mechanical reliability of the design. Direct measurement of structural stress and deformation under operating loads via strain gauges is acknowledged as a limitation and is identified as a priority for future experimental work.

The principal novelty of this study lies in the systematic application of a multi-step FEM-based structural assessment framework to a piston-type wavemaker, an aspect largely absent from the existing literature, which has focused predominantly on hydrodynamic performance. The parametric operational envelope and EN 1993-1-9 fatigue assessment provide quantitative design guidance not previously available for this class of laboratory equipment. All design criteria relating to static strength, stiffness, fatigue life, and dynamic stability were satisfied, and the maximum stroke capacity of ±400 mm establishes a safe design limit under all examined operating conditions. Future work will focus on integrating active wave absorption algorithms to minimise the reflection coefficient and enable generation of JONSWAP and Pierson–Moskowitz spectra. Adapting the open hardware architecture to wave channels of different scales will contribute to strengthening experimental coastal and offshore engineering infrastructure more broadly.

CRediT authorship contribution statement

Semin Kaya: Writing – review & editing, Visualization, Validation, Supervision, Formal analysis, Conceptualization. **Ahmet Kuscuoglu:** Writing – review & editing, Writing – original draft, Visualization, Validation, Supervision, Software, Resources, Project administration, Methodology, Investigation, Funding acquisition, Formal analysis, Data curation, Conceptualization. **Gulenay Alevay Kilic:** Writing – review & editing, Writing – original draft, Visualization, Validation, Supervision, Software, Methodology, Investigation, Formal analysis, Data curation, Conceptualization.

Declaration of competing interest

The authors declare that they have no known competing financial interests or personal relationships that could have appeared to influence the work reported in this paper.

Appendix: Nomenclature

Symbol	Definition	Unit
A	Stroke amplitude	mm
a	Peak sinusoidal acceleration	$mm.s^{-2}$
DAF	Dynamic amplification factor	-
E	Young's modulus	MPa
f	Operating frequency	Hz
F(t)	Time-dependent load vector	N
FS	Factor of safety	-
fn	First natural frequency	Hz
g	Gravitational acceleration (9806.6)	$mm.s^{-2}$
H	Wave height	M
[K]	Global stiffness matrix	$N.mm^{-1}$
[M]	Mass matrix	kg
[C]	Damping matrix	$N.s.mm^{-1}$
p(z)	Hydrostatic pressure at depth z	$N.mm^{-1}$
r	Frequency ratio (f/fn)	-
SM	Safety margin	-
SR	Stiffness ratio	-
T	Wave period	s
t	Plate thickness	mm
u	Nodal displacement vector	mm

(*continued on next page*)

(*continued*)

Symbol	Definition	Unit
$\ddot{u}$	Nodal acceleration vector	$mm.s^{-2}$
$\dot{u}$	Nodal velocity vector	$mm.s^{-1}$
w_{max}	Maximum deflection	mm
z	Water depth	m
$\Delta\sigma$	Stress range	MPa
σ_v	Von Mises stress	Mpa
σ_y	Yield strength	Mpa
φ	Mode shape vector	-
ω	Natural angular frequency	$rad.s^{-1}$
ρ	Water density	$kg.m^{-3}$
Acronyms		
APDL	ANSYS Parametric Design Language	
DAF	Dynamic Amplification Factor	
FEM	Finite Element Method	
FPGA	Field-Programmable Gate Array	
FS	Factor of Safety	
NWT	Numerical Wave Tank	
OWC	Oscillating Water Column	
SDOF	Single Degree of Freedom	
SM	Safety Margin	
SPH	Smoothed Particle Hydrodynamics	
SR	Stiffness Ratio	
WEC	Wave Energy Converter	

Data availability

Data will be made available on request.

References

[1] Beneduce, M. (2018). Polıtecnıco dı torıno collegıo dı ıngegnerıa meccanıca, aerospazıale, dell'autoveıcolo e della produzıone Corso di laurea in ingegneria meccanica design of a wavemaker for the water tank at the politecnico di torino.

[2] N. Krvavica, I. Ružić, N. Ožanić, New approach to flap-type wavemaker equation with wave breaking limit, Coast. Eng. J. 60 (1) (2018) 69–78, https://doi.org/10.1080/21664250.2018.1436242.

[3] Muarif, V. Halfiani, S. Rusdiana, S. Munzir, M. Ramli, Mathematical model of snake-type multi-directional wave generation, in: IOP Conference Series: Materials Science and Engineering 300, 2018 012047, https://doi.org/10.1088/1757-899X/300/1/012047.

[4] I. Gyongy, J.B. Richon, T. Bruce, I. Bryden, Validation of a hydrodynamic model for a curved, multi-paddle wave tank, Appl. Ocean Res. 44 (2014) 39–52, https://doi.org/10.1016/J.APOR.2013.11.002.

[5] S. Lowell, J. McPhee, R.A. Irani, Plunger-type wavemakers with flow: sensitivity analysis and experimental validation, Appl. Ocean Res. 121 (2022) 103065, https://doi.org/10.1016/J.APOR.2022.103065.

[6] K. Szmidt, B. Hedzielski, Transformation of long waves in a canal of variable section, Arch. Hydroengineering Environ. Mech. 63 (1) (2016) 3–18, https://doi.org/10.1515/HEEM-2016-0001.

[7] C. Beringer, B. Bosma, B. Robertson, Detailed uncertainty analysis and nonlinear effects of wave energy converter experimental testing in regular waves, Ocean Eng. 348 (2026) 123024, https://doi.org/10.1016/j.oceaneng.2025.123024.

[8] T. Hiraishi, R. Azuma, N. Mori, T. Yasuda, H. Mase, A new generator for tsunami wave generation, J. Energy Power Eng. 10 (3) (2016), https://doi.org/10.17265/1934-8975/2016.03.004.

[9] M. Li, An optimal controller of an irregular wave maker, Appl. Math. Model. 29 (1) (2005) 55–63, https://doi.org/10.1016/J.APM.2004.07.008.

[10] B. Nouioui, M. Doğan, Irregular wavemaker (piston type) in a numerical and physical wave tank, Usak Univ. J. Eng. Sci. 5 (2) (2022) 95–116, https://doi.org/10.47137/UUJES.1180866.

[11] C. Krautwald, H. Von Häfen, P. Niebuhr, K. Vögele, D. Schürenkamp, M. Sieder, N. Goseberg, Large-scale physical modeling of broken solitary waves impacting elevated coastal structures, Coast. Eng. J. 64 (1) (2022) 169–189, https://doi.org/10.1016/j.coastaleng.2022.104178.

[12] X. Song, J. Yao, W. Liu, Y. Shu, F. Xu, Numerical generation of solitary wave and its propagation characteristics in a step-type flume, J. Mar. Sci. Eng. 11 (1) (2022) 35, https://doi.org/10.3390/JMSE11010035.

[13] J. Lin, L. Hu, Y. He, H. Mao, G. Wu, Z. Tian, D. Zhang, Verification of solitary wave numerical simulation and case study on interaction between solitary wave and semi-submerged structures based on SPH model, Front. Mar. Sci. 10 (2023), https://doi.org/10.3389/FMARS.2023.1324273.

[14] H.E. Wang, I.C. Chan, Numerical investigation of wave generation characteristics of bottom-tilting flume wavemaker, J. Mar. Sci. Eng. 8 (10) (2020) 769, https://doi.org/10.3390/JMSE8100769.

[15] F. Hess, R.M. Boes, F.M. Evers, Forces on a vertical dam due to solitary impulse wave run-up and overtopping, J. Hydraul. Eng. 149 (7) (2023), https://doi.org/10.1061/JHEND8.HYENG-13200.

[16] M. Canard, G. Ducrozet, B. Bouscasse, Generation of 3-hr long-crested waves of extreme sea states with HOS-NWT solver, in: International Conference on Offshore Mechanics and Arctic Engineering 84386, American Society of Mechanical Engineers, 2020 V06BT06A064, https://doi.org/10.1115/OMAE2020-18930.

[17] J. Orszaghova, P.H. Taylor, A.G.L. Borthwick, A.C. Raby, Importance of second-order wave generation for focused wave group run-up and overtopping, Coast. Eng. 94 (2014) 63–79, https://doi.org/10.1016/J.COASTALENG.2014.08.007.

[18] R. El Koussaifi, A. Tikan, A. Toffoli, S. Randoux, P. Suret, M. Onorato, Spontaneous emergence of rogue waves in partially coherent waves: a quantitative experimental comparison between hydrodynamics and optics, Phys. Rev. E 97 (1) (2018), https://doi.org/10.1103/PHYSREVE.97.012208.

[19] J. Song, H.C. Lim, Study of floating wind turbine with modified tension leg platform placed in regular waves, Energies 12 (4) (2019) 703, https://doi.org/10.3390/EN12040703.

[20] Y. Yu, T. Zhao, M. Duan, T. Zhou, J. Xu, Y. Su, H. Liu, Experimental investigation on the underwater soft yoke mooring system considering sloshing, Sh. Offshore Struct. 14 (3) (2019) 309–319, https://doi.org/10.1080/17445302.2018.1498569.

[21] D.D. Prasad, M.R. Ahmed, Y.H. Lee, Performance improvement of a full-scale oscillating water column device by employing a novel double oscillating water column, Proc. Inst. Mech. Eng. M: J. Eng. Marit. Environ. 239 (3) (2025) 635–648, https://doi.org/10.1177/14750902241299585.

[22] R. Gayathri, J.Y. Chang, C.C. Tsai, T.W. Hsu, Wave energy conversion through oscillating water columns: a review, J. Mar. Sci. Eng. 12 (2) (2024) 342, https://doi.org/10.3390/jmse12020342.

[23] H. Thai Le, H. Hoang Truong, H. Chi Minh City, L. Trung Ward, T. Duc City, Analysis of wind-wave impact on open wave channel systems, J. Phys. (2025) 12033, https://doi.org/10.1088/1742-6596/2949/1/012033.

[24] B. Xu, K. Wei, S. Qin, J. Hong, Experimental study of wave loads on elevated pile cap of pile group foundation for sea-crossing bridges, Ocean Eng. 197 (2020), https://doi.org/10.1016/J.OCEANENG.2019.106896.

[25] B.V. Divinsky, R.D. Kosyan, Spectral structure of surface waves and its influence on sediment dynamics, Oceanologia 61 (1) (2019) 89–102, https://doi.org/10.1016/J.OCEANO.2018.07.003.

[26] S. Yan, Z. Zou, D. Wang, Z. You, Longshore current profiles and instabilities on plane beaches with mild slopes, J. Mar. Sci. Eng. 11 (1) (2023) 172, https://doi.org/10.3390/JMSE11010172.

[27] B. Marin-Diaz, T.J. Bouma, E. Infantes, Role of eelgrass on bed-load transport and sediment resuspension under oscillatory flow, Limnol. Oceanogr. 65 (2) (2020) 426–436, https://doi.org/10.1002/LNO.11312.

[28] X. Zhang, J. Lv, R. Hui, D. He, K. Wang, The hydrodynamic study of the interaction between waves and objects in permeable reef environment, Ocean Eng. 305 (2024) 118000, https://doi.org/10.1016/J.OCEANENG.2024.118000.

[29] D.K. Singh, P. Deb Roy, Study of water wave in the intermediate depth of water using second-order Stokes wave equation: a numerical simulation approach, Sādhanā 47 (1) (2022) 45, https://doi.org/10.1007/s12046-021-01792-0.

[30] K. Yan, H. Dou, J. Oh, D. Seo, Numerical comparison of piston-, flap-, and double-flap-type wave makers in a numerical wave tank, J. Mar. Sci. Eng. 13 (12) (2025) 2273, https://doi.org/10.3390/JMSE13122273.

[31] W. Jia, S. Liu, J. Li, Y. Fan, A three-dimensional numerical model with an L-type wave-maker system for water wave simulations by the moving boundary method, Water 12 (1) (2020) 161, https://doi.org/10.3390/W12010161.

[32] J. Jung, J.H. Hwang, A.G.L. Borthwick, Piston-driven numerical wave tank based on WENO solver of well-balanced shallow water equations, KSCE J. Civ. Eng. 24 (7) (2020) 1959–1982, https://doi.org/10.1007/S12205-020-1875-3.

[33] I.H. Cho, M.H. Kim, Effect of a bottom-hinged, top-tensioned porous membrane baffle on the sloshing reduction in a rectangular tank, Appl. Ocean Res. 104 (2020) 102345, https://doi.org/10.1016/j.apor.2020.102345.

[34] H. Jung, H. Ouro-Koura, A. Salalila, M. Salalila, Z.D. Deng, Frequency-multiplied cylindrical triboelectric nanogenerator for harvesting low frequency wave energy to power ocean observation system, Nano Energy 99 (2022) 107365, https://doi.org/10.1016/j.nanoen.2022.107365.

[35] J. Orszaghova, A.G.L. Borthwick, P.H. Taylor, From the paddle to the beach-a Boussinesq shallow water numerical wave tank based on Madsen and Sørensen's equations, J. Comput. Phys. 231 (2) (2012) 328–344, https://doi.org/10.1016/j.jcp.2011.08.028.

[36] H. Dong, S. Yang, Y. Fang, M. Liu, Solitons, cnoidal waves and nonlinear effects in oceanic shallow water waves, Fractal Fract. 9 (5) (2025) 305, https://doi.org/10.3390/fractalfract9050305.

[37] B. Demircan, S. Bıçakçı, E. Akyüz, Position control of hydraulic servo cylinder for wave channel, Konya J. Eng. Sci. 13 (1) (2025) 260–276, https://doi.org/10.36306/konjes.1571870.

[38] F. Tolun, Evaluation of welding parameters effects in friction stir welding of AZ31B Mg alloy, Met. Mater./Kov. Mater. 60 (2) (2022), https://doi.org/10.31577/km.2022.2.109.

[39] B. Demircan, T. Yaren, E. Akyüz, S. Bıçakçı, Modeling of an electro-hydraulic system for wave generation in a wave channel, Balk. J. Electr. Comput. Eng. 13 (3) (2025) 325–337, https://doi.org/10.17694/bajece.1622216.

[40] P.C. Kohnke, Ansys. Finite Element Systems: a Handbook, Springer Berlin Heidelberg, Berlin, Heidelberg, 1982, pp. 19–25.

[41] M. Okereke, S. Keates, Finite element mesh generation. Finite Element Applications. Springer Tracts in Mechanical Engineering, Springer, Cham, 2018, https://doi.org/10.1007/978-3-319-67125-3_6.

[42] G.A. Kilic, CFD-based thermo-hydraulic performance analysis of energy transfer capacity enhancement in intercoolers for hydrogen systems considering operating conditions and flow alignment, Energy Convers. Manag. 343 (2025) 120221, https://doi.org/10.1016/j.enconman.2025.120221.

[43] J. Bonet, T.S. Lok, Variational and momentum preservation aspects of smooth particle hydrodynamic formulations, Comput. Methods Appl. Mech. Eng. 180 (1) (1999) 97–115, https://doi.org/10.1016/S0045-7825(99)00051-1.

[44] F. Naeim, Dynamics of structures—theory and applications to earthquake engineering, Earthq. Spectra 23 (2) (2007) 491–492, https://doi.org/10.1193/1.2720354.

[45] European Committee for Standardization (CEN), Eurocode 3: Design of Steel Structures, Part 1-9: Fatigue. EN 1993-1-9:2005, CEN, Brussels, 2005.

[46] J. Tedesco, W.G. McDougal, C.A. Ross, Structural Dynamics, Pearson Education, London, UK, 2000.

[47] S.S. Rao, Vibration of Continuous Systems, John Wiley & Sons, 2019.

[48] S. Çelik, F. Tolun, Effect of double-sided friction stir welding on the mechanical and microstructural characteristics of AA5754 aluminium alloy, Mater. Test. 63 (9) (2021) 829–835, https://doi.org/10.1515/mt-2021-0009.